

AD-A258 693



ION PAGE

Form Approved
OMB No. 0704-0188

Public
Order
Collect
Data

Page 1 now for release, including the time for reviewing instructions, searching existing data sources, the collection of information, Send comments regarding this burden estimate or any other aspect of this Washington Headquarters Services, Directorate for Information Operations and Reports, 1215 Jefferson Management and Budget, Paperwork Reduction Project (0704-0188), Washington, DC 20543.

1. AGENCY USE ONLY (Leave blank) 2. REPORT DATE: Nov. 19, 1992 3. REPORT TYPE AND DATES COVERED: Final 2/1/91-8/14/92

4. TITLE AND SUBTITLE
Theoretical and STM Studies of the Electronic Structure of Metal/Semiconductor/Hydrogen Systems

5. FUNDING NUMBERS
~~SCRD123~~
AFOSR 91-0164

6. AUTHOR(S)
Prof. Walter C. Ermler

7. PERFORMING ORGANIZATION NAME(S) AND ADDRESS(ES)
Stevens Institute of Technology
Hoboken, NJ 07031

8. PERFORMING ORGANIZATION REPORT NUMBER
AFOSR-91-0164
5-27081

9. SPONSORING/MONITORING AGENCY NAME(S) AND ADDRESS(ES)
AFOSR/NE
Rm. 410
Bldg. 3
DC 20332

10. SPONSORING/MONITORING AGENCY REPORT NUMBER
2301/A7

11. SUPPLEMENTARY NOTES

DTIC
ELECTE
DEC 29 1992
S A D

12. DISTRIBUTION/AVAILABILITY STATEMENT
unlimited

13. ABSTRACT (Maximum 200 words)
The structure of atomic clusters is investigated using methods of ab initio quantum chemistry in conjunction with scanning tunneling microscopy (STM). Gold sols are imaged via STM and their sizes characterized. Atomic resolution reveals facets, steps, and reconstructed surfaces of the sols. STM images of graphite surfaces are characterized by two mechanisms: a twisted top layer configuration and a graphite-flake-contaminated tip. A crystalline tip model reproduces anomalous long range periodicity, attributed to defect-mediated tip-substrate convolution. Ab initio calculations of electronic states of a 135 atom Be cluster show bulk behavior for many properties centered at the middle of the cluster. The density of states agrees well with band theory models. Full spin-orbit CI calculations of the electronic spectrum and potential energy curves of LiBe, including Rydberg states, are definitive and accurate. A procedure for the incorporation of core/valence polarization effects in all-valence electron calculations is presented for use with relativistic effective core potentials. The method allows the treatment of large clusters at the ab initio level including procedures for the inclusion of electron correlation.

This document has been approved for public release and sale; its distribution is unlimited.

14. SUBJECT TERMS

15. NUMBER OF PAGES: 74
16. PRICE CODE

17. SECURITY CLASSIFICATION OF REPORT

18. SECURITY CLASSIFICATION OF THIS PAGE

19. SECURITY CLASSIFICATION OF ABSTRACT

20. LIMITATION OF ABSTRACT

Table of Contents

1.	Cover and Title Page	i
2.	Table of Contents	ii
3.	Research Objectives and Status of Research	1
	Publication 1	3
	On the interpretation of scanning tunneling microscope images showing anomalous periodic structures	
	Publication 2	21
	Ab initio studies of the electronic structure and density of states of metallic beryllium	
	Publication 3	36
	Spin-orbit configuration-interaction study of valence and Rydberg states of LiBe	
	Publication 4	62
	Ab initio REP-based relativistic core/valence polarization operator	
4.	Publications	73
5.	Professional Personnel	73
6.	Interactions	74
7.	New Discoveries, Inventions or Patents	74
8.	Additional Statement	74

3. Research Objectives and Status of Research

Grant AFOSR-90NP123

Theoretical and STM Studies of the Electronic Structure of Metal/Semiconductor/Hydrogen Systems

Walter C. Ermler, Professor of Chemistry and Physics
Department of Chemistry and Chemical Engineering
Stevens Institute of Technology
Hoboken, New Jersey 07030
(201) 216-5520

Final Report

A research project to study the physical properties of gold sols using the scanning tunneling microscope (STM) was carried out by a graduate student receiving support through this grant under the direction of the PI. The experimental work was completed within the duration of the grant and the student is finalizing his dissertation and is planning to defend it this winter. A copy of the dissertation will be forwarded to the AFOSR upon its final approval. The research involved the deposition of colloidal gold onto highly ordered pyrolytic graphite and imaging using the STM. Two preparations were used involving the citrate reduction of gold tetrachloroaurate yielding highly monodispersed sols. One sol synthesized at 373 K was found to have a mean particle size of 16.64 nm with a spread of 3.84 nm from an analysis of 194 particles. The mean diameter-to-height ratio was determined to be 8.0 ± 4.6 nm. A gold sol synthesized at 346 K yielded a mean particle diameter of 17.55 ± 4.30 nm and diameter-to-height ratio of 8.4 ± 2.2 . Examination of the particle surfaces using the STM revealed atomic resolution of facets, steps and reconstructed surfaces. The lattice constants agreed well with independently determined bulk values.

Four additional related projects were partially supported by this grant. The first involved the study of the nature of STM images on graphite surfaces and resulted in a publication in The Journal of Physical Chemistry on interpretation of apparent long range order. Computer simulations were compared with actual STM data to lend credence to the postulated model. This paper is given in the following section.

92 12 28 077

92-32902



The second project dealt with the interpretation of large metal clusters in terms of bulk properties. A cluster of 135 beryllium atoms was treated using effective core potentials (EP) to replace the Be 1s electrons and ab initio Hartree-Fock-Roothaan SCF-MO theory to describe the remaining 270 valence electrons. Ionization potentials, binding energies, orbital energies, and one-electron properties were calculated for a range of electronic states. The ground state valence wave function was also used to calculate the density of states for comparison to band structure calculations. The convergence of properties to bulk values was determined based on values of properties centered at the atom in the middle of the cluster. The complete study, published in the International Journal of Quantum Chemistry, is discussed under Publication 2 below.

The use of EPs to replace the 1s core electrons of Li and Be was the basis of full spin-orbit configuration interaction calculations on the prototype simplest heteronuclear metal cluster LiBe and three lowest-lying cations. The complete electronic spectrum including the 3s, 3p, 3d and 4s Rydberg states of Li was calculated and compared to available experimental results. Excitation energies agree well with experiment and the predicted spectrum and potential energy curves are definitive. The results were published in The Journal of Chemical Physics and are given below under Publication 3.

The LiBe study was an initial example of a method devised for treating few-electron systems at a high level of theory. An extension of the method to include core/valence polarization is shown below under Publication 4 and will be published in the Proceedings of a NATO/ASI Institute. A method for deriving a core/valence polarization operator that includes spin-orbit and other relativistic effects is presented. This operator can be used together with relativistic effective core potentials to reduce the number of valence electrons that must be explicitly considered to the smallest possible number.

The four projects were completed during the period of the one-year AFOSR award. They all contributed to a deeper understanding of the fundamental nature of interatomic interactions. The work was published and the benefits to the students involved in the projects were many fold. Results were also presented at meetings and in departmental seminars (Section 6).

ACCESSION FOR	
NTIS	<input checked="" type="checkbox"/>
CRA&I	<input type="checkbox"/>
DTIC	<input type="checkbox"/>
TAB	<input type="checkbox"/>
Unannounced	<input type="checkbox"/>
Justification	
By _____	
Distribution /	
Availability Codes	
Dist	Avail
A-1	General

On the Interpretation of Scanning Tunneling Microscope
Images Showing Anomalous Periodic Structures

Makoto Sawamura, John F. Womelsdorf, Walter C. Ermler.

Department of Chemistry and Chemical Engineering,

Department of Physics and Engineering Physics,

Stevens Institute of Technology,

Hoboken, New Jersey 07030

Abstract

Scanning tunneling microscope images of graphite surfaces containing anomalous long-range structures are shown to originate from two distinct mechanisms. A twisted top layer graphite configuration is shown to produce super structures with divergent periods from 101 Å to 760 Å and decaying amplitudes. A graphite-flake-contaminated tip is shown to yield long range ordered arrays with constant periodicity, constant amplitudes, and abrupt domain termination. These arrays are consistently reproduced using a theoretical crystalline tip model. Hexagonal closed-packed patterns with periods ranging from 48 to 220 Å are experimentally observed and theoretically simulated using this model. The origin of such images is discussed in detail and a class of the anomalous long-range periodicities observed are attributed to a defect-mediated tip-substrate convolution phenomenon.

Introduction

Since its introduction,¹ the scanning tunneling microscope (STM) has provided direct images of surfaces of various conductive materials.²⁻⁴ A compelling feature of STM is its ability to investigate local surface features of various substrates with atomic resolution. However, the detailed interpretation of some classes of images is not sufficiently understood. For example, anomalous long-range periodicity is occasionally reported to be observed on highly oriented pyrolytic graphite (HOPG)⁵⁻⁸ and gold.³ Although the existing theories of the STM measurement do not completely explain these phenomena, there are several qualitative explanations for the long-range periodicity.^{6,7}

Mizes et al. first invoked the possibility of using multiple tips for an STM model to explain various anomalous surface images of HOPG.⁹ Albrecht et al. attributed anomalous long-range periodicity on a graphite surface to an artifact due to isolated multiple tips simultaneously scanning two grains in which crystal axes are twisted with respect to one another.⁶ On the other hand, similar anomalous long-range periodicity is also believed to result from a twisted top layer configuration resulting in an STM image described as a moire fringe pattern.⁷ Such anomalous images are described by constant periodicity and amplitude with abrupt domain termination.

The origin of anomalous long-range structures observed on HOPG by STM is addressed in this work. It is clearly shown that a twisted top layer HOPG configuration explains divergent long range structures but is inconsistent with ordered arrays observed on HOPG. Based on a fundamentally stable model of a polyatomic crystalline STM tip configuration, which is logically extended to graphite-contaminated tips, STM images of such ordered arrays are correctly described. This model shows that such images are an artifact of the measurement process and not a property of the surface. The computational simulation based on the present model is found to be consistent with the experimentally observed anomalous long-range order in STM images.

Theory

Many of the existing theories of STM have assumed that an ideal tip is comprised of a single atom at the position nearest to the surface,¹⁰⁻¹² although the stability of the single atomic tip has been questioned.¹³ In recent studies by transition electron microscopy, crystalline structures were observed on the surfaces of STM tips.¹⁴ The polyatomic STM tip model given here derives from currently accepted fundamental assumptions¹⁵ containing the following components. First, an STM tip is assumed to possess a finite crystal structure, which is inherently more stable than a single atom tip configuration. Second, the net tunneling current is defined as the summation of currents

due to tunneling from each atom on the tip to every atom of the sample substrate. The intensity of the current between an atom on the sample and an atom on the tip is described by the Tersoff and Hamann relation in the low bias limit.¹⁶

The net tunneling current from an STM tip positioned at the coordinate (l, k) to the surface can be defined by:

$$I_{total} = \sum_i \sum_j I_{ij}(l, k),$$

$$I_{ij}(l, k) = A \exp[-\alpha \{(x_{ij} - x_{lk})^2 + (y_{ij} - y_{lk})^2 + (z_{ij} - z_{lk})^2\}^{1/2}],$$

where $I_{ij}(l, k)$ is the tunneling current between an atom located at (x_{ij}, y_{ij}, z_{ij}) on the surface and an atom at (x_{lk}, y_{lk}, z_{lk}) on the STM tip, and α depends on the characteristics of the materials of both the tip and surface. The net current is a summation of all tunneling occurrences resulting in the superimposed image. In the case where the sample substrate has a low workfunction region, for example a step edge,¹⁷ it has been shown that the defect may act as a pseudo-atom and be scanned by the STM tip surface.¹⁸ In this instance the atoms on the tip will periodically scan the point defect producing a tip self-image. The analysis presented in this paper will assume that graphite step edges constitute low barrier height regions. Consequently, it is therefore not surprising that in many cases long-range periodicity has been observed adjacent to a surface defect.⁵⁻⁸

Results

Figure 1 displays an image of a long-range super structure observed on HOPG in air which is attributed to a twisted top layer HOPG configuration. The bias voltage was 50 mV and the tunneling current 1.0 nA. The data was obtained using a $\text{Pt}_{0.8}\text{Ir}_{0.2}$ tip. The observed periodicities range from 101 Å to 760 Å smoothly diverging along the sides of the triangle domain. This image clearly describes the divergent nature of the anomalous image which is consistent with a twisted layer mechanism based on the discussion below.

Figure 2a displays an STM image of a long-range periodic pattern on a freshly cleaved HOPG surface probed in air with a $\text{Pt}_{0.8}\text{Ir}_{0.2}$ tip. The bias voltage was 150 mV and the tunneling current set at 1.0 nA. The STM was operated in constant height mode. A hexagonal close-packed pattern with long-range periodicity of 60 ± 1 Å is apparent. It is noted that atomic resolution can be observed throughout the image. The large hexagons and atomic hexagons are rotated with respect to one another by approximately 30 degrees. This image displays a portion of the surface which contains a long-range periodic domain lying along a step edge.

A 3-dimensional simulation for the experimental image of Figure 2a based on a tip-substrate convolution is shown in Figure 2b. The sample substrate was taken as a hexagonal close-packed surface with an atomic distance of 2.45 Å

corresponding to the HOPG (0001) surface in keeping with known α and β inequivalences on graphite.¹⁹ Both the sample substrate and tip are comprised of $25 \times 35 = 875$ atoms. In this simulation, a graphite (0001) surface was assumed for both the tip and the sample substrate and includes β atoms only. The substrate contains a low workfunction defect in the scanned region. The coordinate axes of the tip and sample are rotated relative to one another by 2.3 degrees. A large periodicity is clearly observed in Figure 2b having a period of 60 Å. This corresponds to the experimentally obtained result of 60 ± 1 Å shown in Figures 2a.

It is clearly plausible to envisage a graphite surface for an STM tip instead of a metal surface since the tips are known to pick up graphite flakes.^{20,21} After scanning a graphite surface for a sufficient period of time the graphite is observed to grow hair-like on the STM tip. Since these graphite hairs must be in contact with the surface substrate as they grow, the graphite surface contributing to the net tunneling current may be nearly parallel to the sample substrate. This is conceptually similar to a paintbrush that is placed in close contact with a planar surface which will relax the bristles to a nearly coplanar configuration in order to reduce the repulsive forces. Such a graphite flake results in a large periodic tip surface which explains the large ordered superstructure. The super periodicity s for the graphite substrate and tip is described by $s = a/2\sin(\theta/2)$ where a is the graphite β - β distance and θ the rotational angle of the

crystal axis of the tip with respect to the substrate crystal axis. A similar expression for the graphite super periodicity can be found in the work of Kuwabara et al.⁷ However, the mechanism presented here is completely distinct from their model. The similarity between both formulations lies only in their geometric descriptions.

Discussion

A twisted top layer model of HOPG may be divided into two cases. The first case is that of a large flake which is rotated at some angle relative to the basal plane of the second layer. The second case corresponds to a region of the top layer basal plane which has been rotated in a similar fashion but represents a small domain of an otherwise commensurate layer. The former configuration is dismissed since it requires that the domain of the anomalous structure be contained within the step edges of the flake. Such structures have not been reported. The latter, however, does not demand a step edge perimeter although the presence of such a step edge may indeed be present.

Although it has been reported that a twisted top layer configuration results in long range periodic STM images, such reports show distinct boundaries between the super structure and the normal graphite lattice.⁷ There is usually a defect associated with one boundary with the others terminating abruptly. This suggests that the

rotation, which has been proposed as an explanation for such features, also terminates abruptly. This logically results in a tearing of the top layer, which is not experimentally observed.

However, if a top layer basal plane contains two domains, one twisted with respect to the underlying layer and the other left unperturbed, then the maximum rotation present in one domain must be damped to zero rotation in the other domain. This transition will avoid cleaving the basal plane which contains the two domains, but requires that the angle of rotation changes over the transition or damped region. Therefore, the predicted periodicity cannot be constant over this region. Furthermore, the effective angle of rotation over this transition region is gradually reduced as the unperturbed domain is approached. As the large periodicity increases, the rotational angle decreases according to $S = a/2\sin(\theta/2)$ as proposed by Kuwabara et al.⁷ Since the wavelength of the long-range periodicity approaches infinity at infinitesimal rotation angles, the boundary shared by the two domains is described by the limit of the diverging superstructure. Figure 1 displays just this behavior. The superstructure is described by an array whose long-range period diverges as the normal graphite lattice is recovered accompanied by the amplitude of the array damping to zero. Therefore, Figure 1 is consistent with a twisted top layer model.

It was shown in our previous study that if the tip and sample have different nearly parallel crystalline structures, and there is no low workfunction defect on the surface corresponding to the smaller atomic lattice, the observed image is a periodic pattern of the surface containing the smaller periodicity.¹⁸ This result may be apparent if translationally symmetric properties of the system are considered in the scanning process. Albrecht et al. employed isolated multiple tips scanning two grains twisted relative to one another.⁶ However, images having two domains exhibiting both normal atomic resolution and long-range periodicities along the grain boundaries cannot be explained using their model (Figure 2 a). First of all, it is unlikely that two minitips resolving atomic periodicity contribute to the net tunneling current on a nearly equal basis. Second, it is unclear how distinct well defined boundaries will emerge if the grain boundary is irregular as was seen in Ref 6. Finally, this model does not address why such long-range structures are not observed on other surfaces which exhibit grain boundaries.

Long-range order over three different steps, where these steps produced identical long-range spacings, is shown in Figure 3. The surface was scanned in air with a $\text{Pt}_{0.8}\text{Ir}_{0.2}$ tip under 20.1 mV bias voltage and 1.0 nA tunneling current in constant height mode. The period is 52 ± 2 Å. This image is attributed to a tip-substrate convolution resulting from a polyatomic STM tip scanning an HOPG substrate which contains a low workfunction defect.

Kuwabara et al., however, attributed the observed long-range periodicity to the presence of a twisted top layer of graphite.⁷ If a twisted first layer model is used for the interpretation of this image, it is necessary to assume that every step containing the identical long-range periodicity is rotated by the same angle with respect to the next lower layer. Furthermore, as discussed above, it is unclear how distinct boundaries and constant periodicity can be explained by this method. Consequently, this phenomenon cannot be justified in general using a twisted first layer model. In addition independent surface techniques would not detect such long-range order since it results as an artifact of the STM measurement process.

Conclusions

Anomalous long-range periodic structures observed on HOPG may be divided into two classes. The first class of images results from a twisted top layer configuration. The nature of these images is in stark contrast with those previously described. STM images derived from twisted top layer HOPG structures are identified by a long-range super structure whose periodicity diverges with a decaying amplitude as the non twisted domain is approached.

The second class of images result from a crystalline or graphite contaminated tip that encounters a low workfunction surface defect. These images are fundamentally different in that they have constant long-range periods, constant

amplitudes, and abrupt domain boundary termination. Such images are indicative of extensive tip contamination. It should be noted that all the images of this type which have been encountered in our laboratory may be successfully interpreted based on this model.

Acknowledgments

This research was supported in part through the Air Force Office of Scientific Research and by the National Science Foundation under grant No. CHE-8912674. We are also grateful to Prof. D. M. Kalyon and Dr. J. Wang for the use of their Silicon Graphics Iris facility to implement our model.

References:

- (1) Binnig, G.; Rohrer, H.; Gerber, Ch.; Weibel, E. *Phys. Rev. Lett.* 1982, 40, 57.
- (2) Binnig, G. K.; Rohrer, H.; Gerber, Ch.; Stoll, E. *Surf. Sci.* 1984, 144, 321.
- (3) Kaiser S. J.; Jaclevic, R. C. *Surf. Sci.* 1987, 182, 1227.
- (4) Trevor, D. J.; Chidsey, C. E. D.; Loiacono, D. N. *Phys Rev. Lett.* 1989, 62, 929.
- (5) Lyding, J. W.; Hubacek, J. S.; Gammie, G.; Skala, S.; Brokenbrough, R.; Shapley, J. R. Keyes, M. P. *J. Vac. Sci. Technol.* 1988, A 6, 363.
- (6) Albrecht, T. R.; Mizes, H. A.; Nogami, J.; Park, Sang-il; Quate, C. F. *Appl. Phys. Lett.* 1988, 52, 362.
- (7) Kuwabara, M.; Clarke, D. R.; Smith, D. A. *Appl. Phys. Lett.* 1990, 56, 2396.
- (8) Womelsdorf, J. F.; Sandroff, C. J.; Ermler, W. C. *J. Phys. Chem.* 95, 503 (1991).
- (9) Mizes, H. A.; Park, Sang-il; Harrison, W. A. *Phys. Rev.* 1988, B 36, 4491.
- (10) Lang N. D. *Phys. Rev. B* 1986, 34, 5947.
- (11) Ciraci, S.; Baratoff, A. Batra, I. P. *Phys. Rev B* 1990, 41, 2763.
- (12) Ohnishi, S.; Tsukada, M. *Solid State Comm.* 1989, 71, 391.
- (13) Pethica, J. B. *Phys. Rev. Lett.* 1986, 57, 3235.
- (14) Garnæs, J.; Kragh, F.; Mørch, K. A.; Thölén, A. R. *J. Vac. Sci. Technol.* 1990, A 8, 441.
- (15) Hamers, R. J. *Annu. Rev. Phys. Chem.* 1989, 40, 531.

- (16) Tersoff, J.; Hamann, D. R. *Phys. Rev. Lett.* 1983, 50, 1998.
- (17) Krahl-Urban, B.; Wagner, H.; Buts, R.; *Surf. Sci.* 1980, 93, 423.
- (18) Womelsdorf, J. F.; Sawamura, M.; Ermler, W. C. *Surf. Sci. Lett.* 1991, 241, 11.
- (19) Binning, G.; Fuchs, H.; Gerber, Ch.; Rohrer, H.; Stoll, E.; Tosatti, E. *Europhys. Lett.* 1986, 1, 31.
- (20) Colton, R. J.; Baker, S. M.; Driscoll, R. J.; Youngquist, M. G.; Baldeschwieler, J. D.; Kaiser, W. J. *J. Vac. Sci. Technol.* 1988, A 6, 349.
- (21) Abraham, F. F.; Batra, I. P. *Surf. Sci. Lett.* 1989, 209, 125.

Figure Captions:

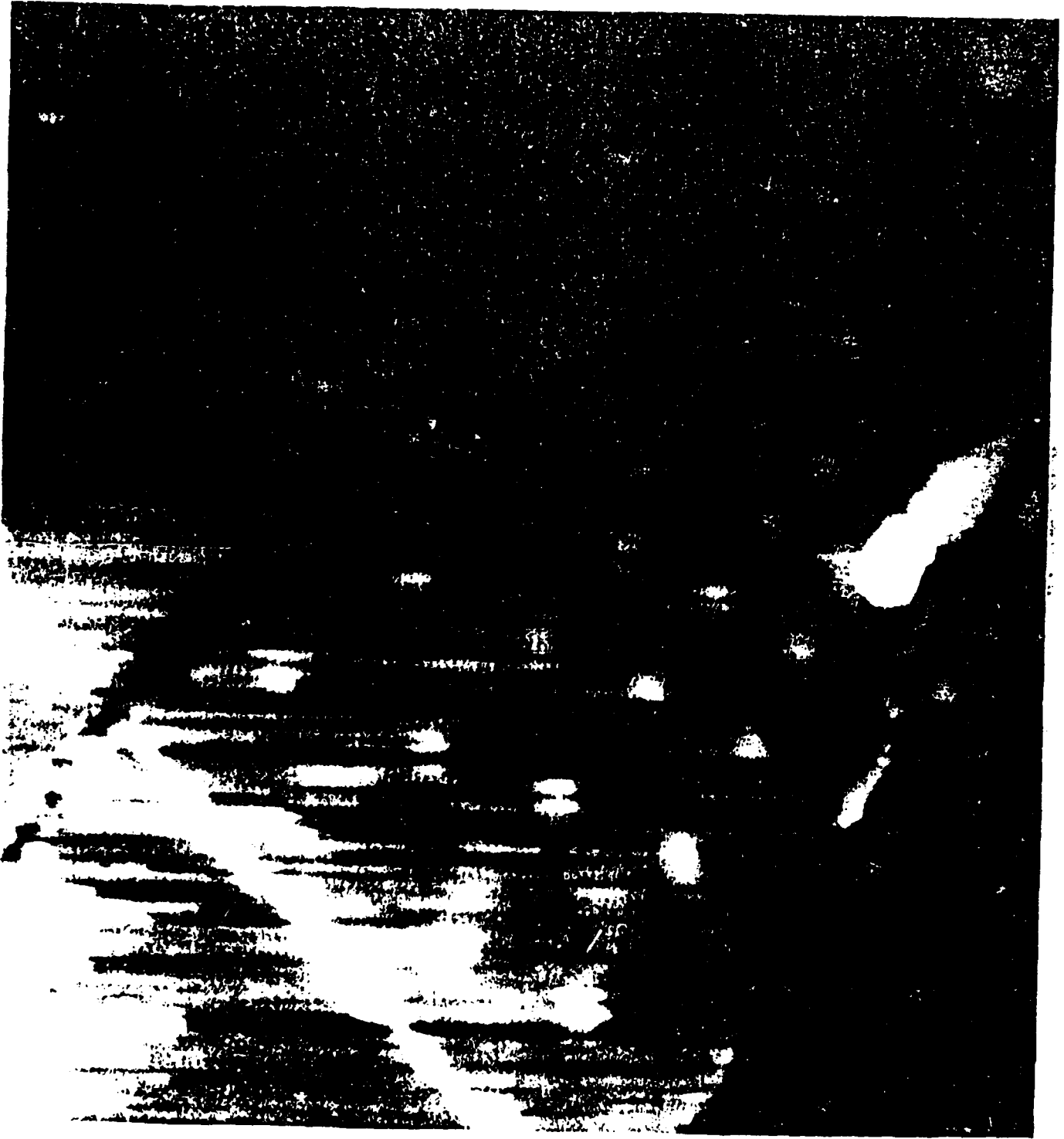
Figure 1. A 2500 Å x 2500 Å experimental image of an HOPG substrate with bias voltage of 50 mV. The long-range period diverges along the edge of the triangle domain, ranging from 101 Å to 760 Å.

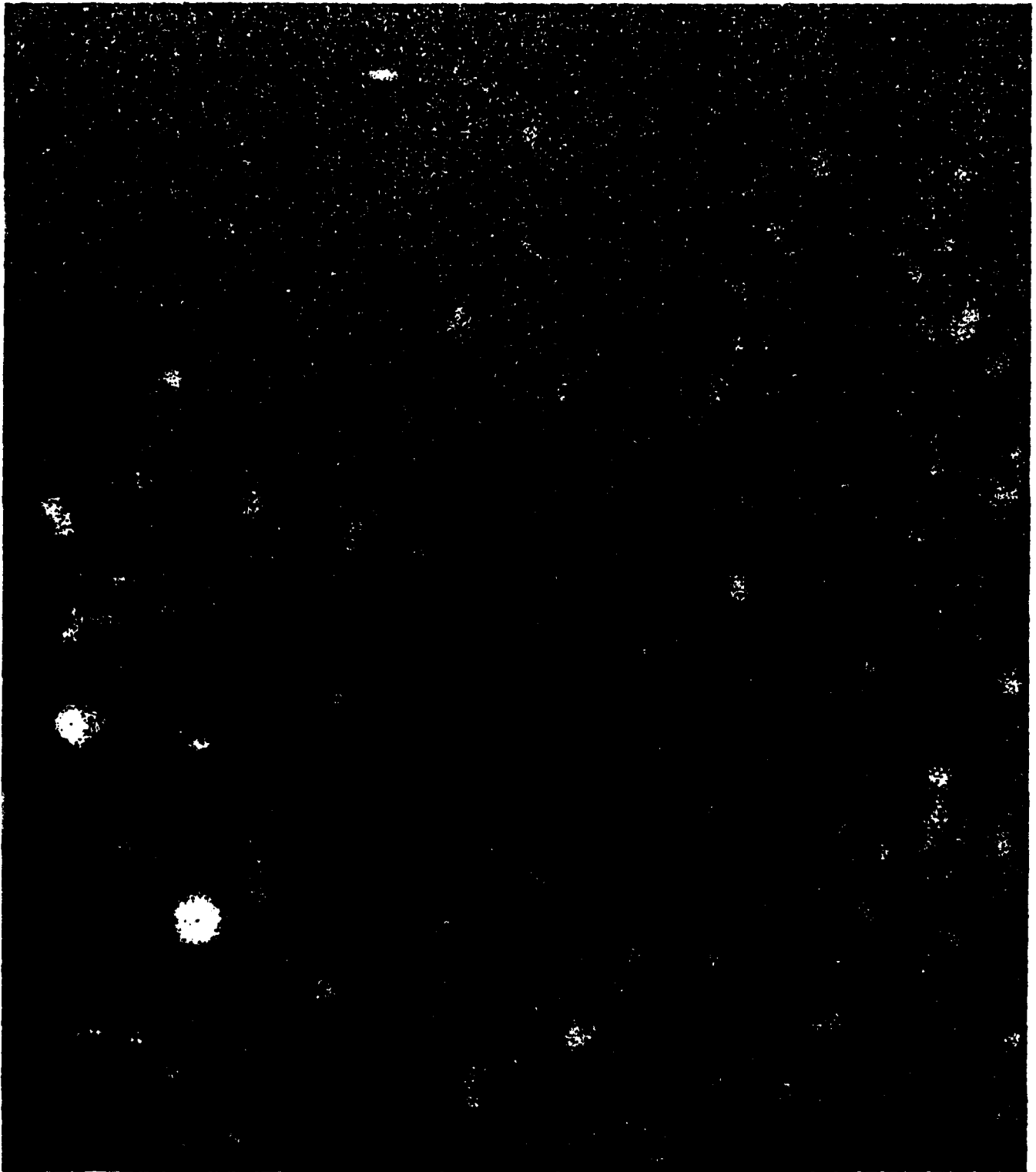
Figure 2 a. A 160 Å x 120 Å experimental image of an HOPG substrate, scanned in air with bias voltage of 150.1 mV. The dark areas comprise a large hexagonal closed-packed pattern with a period of 60 +/- 1 Å. The atomic resolution is also observed.

Figure 2 b. A simulation of a graphite (0001) surface scanned by a graphite (0001) surface comprising a tip. The size of the image is 58.8 Å x 83.3 Å. The long-range period of 60 Å is clearly reproduced. The image is horizontally compressed by 37.4 %.

Figure 3. A 4200 Å x 4200 Å experimental image of an HOPG substrate, scanned in air with bias voltage of 20.1 mV. The long-range period of 52 +/- 2 Å is observed in two domains over three steps.

Figure 1





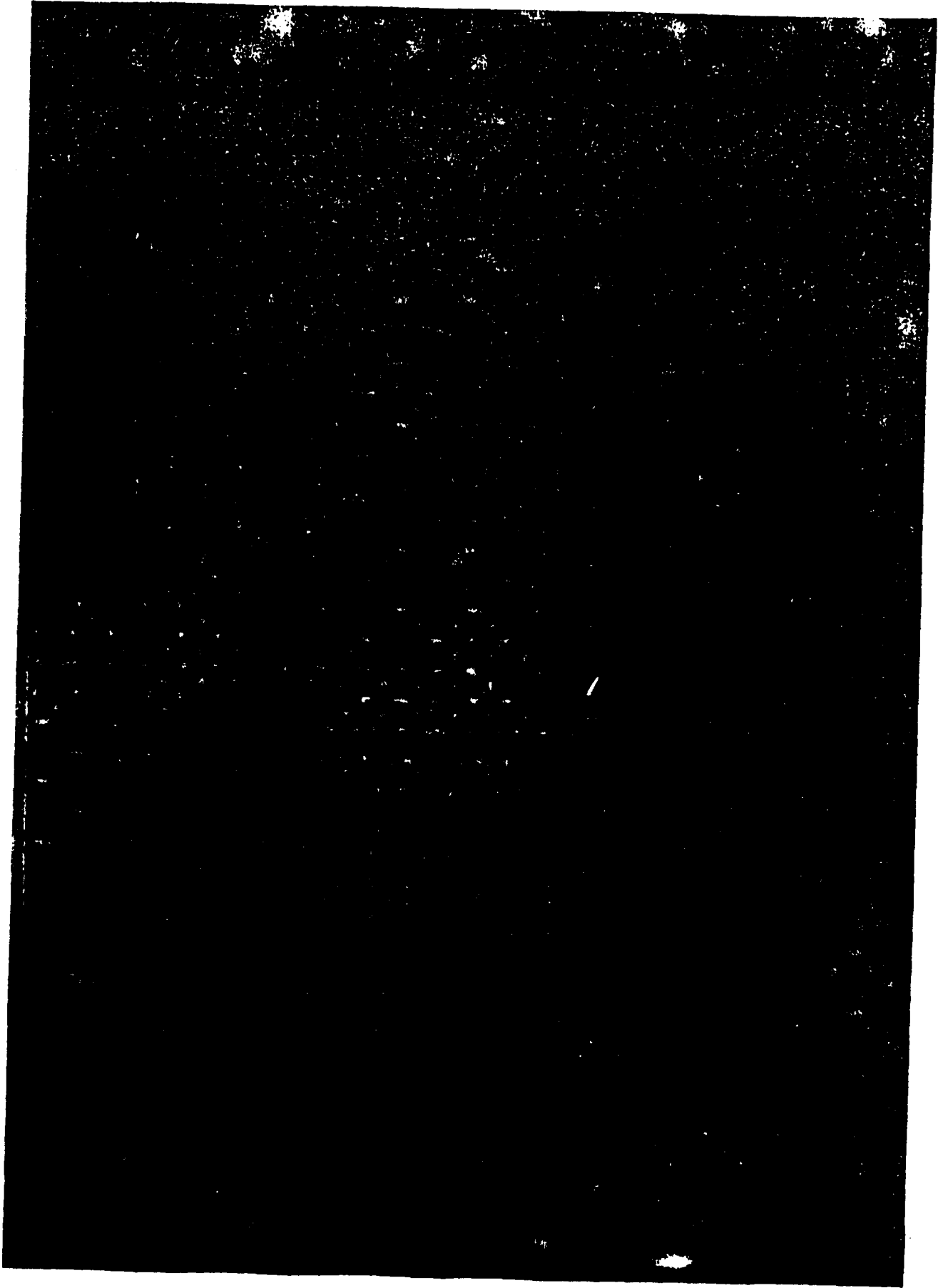




Fig. 3

Ab Initio Studies of the Electronic Structure and Density of States of Metallic Beryllium

R. B. ROSS, W. C. ERMLER, C. W. KERN, AND R. M. PITZER

Department of Chemistry, The Ohio State University, Columbus, Ohio 43210

Abstract

Hartree-Fock-Roothaan studies are reported for low-lying electronic states of metallic beryllium as modeled by a moiety of 135 beryllium atoms. The system corresponds to 16 coordination shells of a central Be with internuclear separations derived from the lattice constants of the bulk metal. The calculations become tractable by use of the full D_{3h} symmetry of the system at both the integrals and self-consistent-field stages and by employing ab initio effective potentials for the 1s electrons of each beryllium atom. Ionization potentials, binding energies, orbital energies, electric field gradients, nuclear-electrostatic potentials, diamagnetic shielding constants, second moments, and Mulliken populations are calculated for selected electronic states. The calculated ionization potential for the lowest state agrees to within 10% of the experimental bulk work function. A density-of-states analysis for that state is reported and compared with band structure calculations.

Introduction

Bulk systems can be modeled employing first-principle quantum chemical studies on large fragments of the bulk provided a sufficient number of atoms are included. Since ab initio quantum chemical calculations on systems of 50-150 atoms are becoming increasingly manageable with current supercomputing technology and systems of larger dimension are likely to become feasible with exploitation of massively parallel systems, it is of interest to test this approach on a bulk system.

In choosing a model system for exploratory theoretical study, the availability of experimental results is an important criterion. In addition to the fact that many of its bulk properties as well as its electric field gradient are known, beryllium has attracted a considerable amount of theoretical interest. Previous large fragment, cluster, or band theory studies include ab initio Hartree-Fock-Roothaan (HFR) studies on fragments of the bulk metal of up to 87 atoms [1-5], HFR studies on a cluster of 55 atoms [6], a Hartree-Fock band theory study [7], local density approximation band theory studies [8, 9], and orthogonalized plane wave band theory studies [10, 11].

In this work Hartree-Fock-Roothaan calculations are reported for selected states of metallic beryllium as modeled by a moiety of 135 beryllium atoms. A multiconfiguration self-consistent field (MCSCF) calculation is also reported to investigate the mixing of two low-lying states. The system, shown in Figure 1, is a fragment of bulk beryllium metal and corresponds to 16 coordination shells of atoms around a central beryllium atom (13 shells if bulk beryllium were perfect hcp). This work is an extension of previous studies on metal fragments of 13 through 87 beryllium atoms [1-5]. Results are compared to experiment, the earlier fragment studies, and studies employing theoretical methods based on band theory.

Calculations

The HFR calculations become tractable through use of the full D_{3h} point group symmetry of the system and ab initio effective potentials to replace the 1s core electrons of each beryllium atom. A contracted $(3s2p)/(2s1p)$ Gaussian-type function (GTF) basis set optimized in a previous study [1] has been employed to represent the valence electrons. In the integrals step of the study, 2×10^8 integrals were computed requiring 43 h of Cray Y-MP8 supercomputer CPU time; this would be a considerable amount on a one-processor system, however, optimal use of multiprocessor systems such as the Cray Y-MP8 can make such calculations routinely manageable. A comparable all-electron study with a $[9s5p]$ primitive GTF basis set and without the use of symmetry or effective potentials would require the computation of 2×10^{12} integrals. Details of the specific reductions

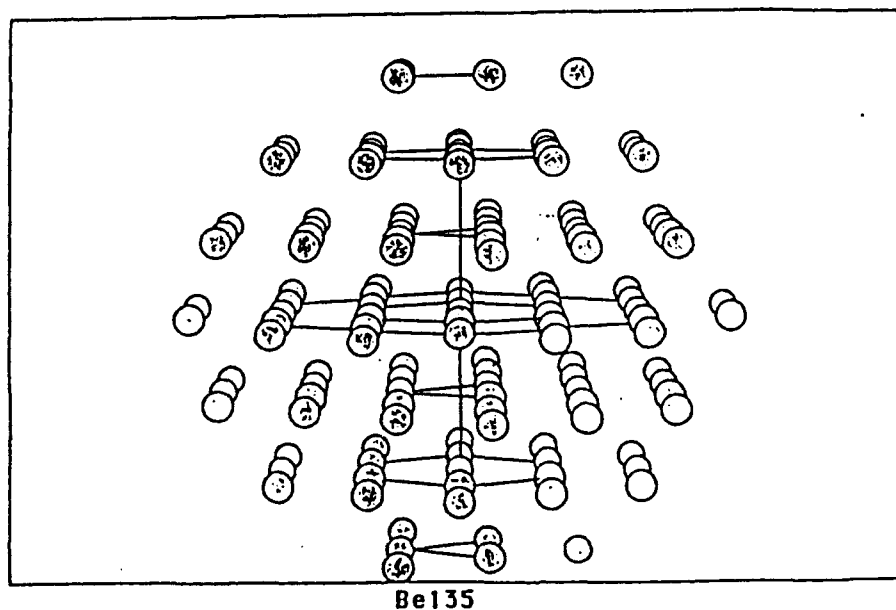


Figure 1. Be_{135} : 16 coordination shells of a central Be atom.

in numbers of integrals with use of symmetry and effective potentials have been given in an earlier study [4].

The entire set of two-electron integrals required 4.8 gigabytes of disk space. In subsequent HFR and MCSCF studies, however, only the subset of integrals required for a particular spin state was kept on-line for states of that class. This resulted in a reduction of on-line disk space requirements to a minimum of 3.3 gigabytes.

The procedure followed initially for the HFR studies was to guess a closed-shell electron configuration based on low-lying states found for smaller fragments. Molecular orbital occupations were then adjusted in test calculations until the orbital energies of the highest occupied molecular orbitals (HOMO) for all of the 6 irreducible representations were lower than that for the lowest unoccupied orbital (LUMO) of the fragment. This state was then converged (Table I, state 9) to 10^{-9} a.u. for one- and two-electron energies. The resulting wave function was then used as an initial guess for an exhaustive search for lower-lying states using HOMO/LUMO analyses as a partial guide.

Molecular orbital (MO) occupations and calculated binding energies, ionization potentials, and excitation energies for the ground state and 7 additional lower-lying states converged to 10^{-9} a.u. are shown in Table I. These states correspond to either closed-shell or average-energy-of-configuration states in the case of open-shell MO configurations. The average energy of a single MO configuration is defined as the weighted mean of the energies of all multiplets for the configuration [12]. In earlier studies on fragments of greater than 50 atoms, it was observed that calculated properties, populations, and other quantities are largely insensitive to spin coupling for a given electron configuration [2].

The HFR studies typically required between 300 and 400 iterations to converge each state such that properties were constant to the significant figures reported (10^{-9} a.u. in this case). Each iteration required 136 seconds of Cray Y-MP CPU time. The HFR and MCSCF studies for the various states and ions were all carried out using the "once-computed" integrals data set described above.

While alternative methods such as direct SCF [13] can be performed with smaller disk space requirements, they were not considered in this study because it was planned to investigate a large number of neutral and ion states. Recomputation of the integrals in every case would be required if such direct methods were employed. While the current approach requires the use of more disk space than direct methods, it results in greater flexibility with regard to the investigation of excited states and ions with an appreciable overall CPU time savings.

An MCSCF study was carried out to investigate the mixing of low-lying electronic states. In this case the MO configurations of the ground state and the state obtained by exciting two electrons from highest occupied a_1 molecular orbital of the ground state into the lowest unoccupied a_1 molecular orbital were employed as configurations for the study (states 1 and 8 of Table I). Total energies and configuration interaction coefficients are reported for this study in Table II.

Properties analyses were also carried out for low-lying states as reported in Table I. Those properties included the electric field gradient, nuclear-electrostatic potential, and diamagnetic shielding constant at the central atom, and the

Table I. Highly converged low-lying states of Be₁₁.

No.	Open-shell electrons	State ^a	MO configuration ^b										IP ^c	IP ^d	BE ^e	ΔE ^f
			19a ₁	8a ₁	16a ₂	25 ₁	20 ₁	6a ₁	1P ^g	1P ^h	BE ^e	ΔE ^f				
1	0	¹ A ₁	0	2	0	4	0	2	4.29	4.53	31.7	—	—	—	—	
2	2	Av.	0	1	0	4	1	2	4.22	—	31.7	0.040	—	—		
3	2	Av.	0	0	0	4	2	2	4.21	—	31.7	0.049	—	—		
4	4	Av.	0	2	0	2	2	2	4.15	—	31.6	0.457	—	—		
5	2	³ A ₁	1	1	0	4	0	2	3.48	—	31.6	0.809	—	—		
6	2	Av.	1	1	0	4	0	2	3.47	—	31.5	0.814	—	—		
7	6	Av.	1	1	0	2	2	2	3.28	—	31.5	1.323	—	—		
8	0	¹ A ₁	2	0	0	4	0	2	3.30	3.81	31.4	1.738	—	—		
9	0	¹ A ₁	2	0	0	4	0	2	3.63	3.96	31.0	1.738	—	—		
Exp.	—	—	—	—	—	—	—	—	3.92 ^e	3.92 ^e	75.3 ^h	—	—	—		

^aAv. denotes average of configuration.

^bInner valence MOs (1a₁)²... (18a₁)²(1a₂)²... (7a₂)²(1a₃)²... (15a₂)²(1e₁)⁴... (24e₁)⁴(1e₂)⁴... (18e₂)⁴(1a₇)²... (5a₇)².

^cIonization potential (eV) calculated as the difference between HFK energies of the neutral and singly ionized clusters (ASCF).

^dKoopmans' theorem ionization potential (eV).

^eBinding energy per atom (kcal/mol) relative to atomic SCF energy of -0.95083 a.u.

^fExcitation energy (eV) relative to total valence energy of -135.1804264 a.u.

^gRef. 16.

^hRef. 20.

TABLE II. Multiconfiguration self-consistent field study on Be_{133}

MCSF Study	Configuration interaction coefficients		Total energy (a.u.)
	State 1	State 8	
2-Configuration	0.9997	-0.0230	-135.180602
scf Studies	Molecular orbital configuration ^a		Total energy (a.u.)
Electronic state	$19a_1^i$	$8a_2^i$	
Closed-shell state 1	0	2	-135.180426
Triplet	1	1	-135.150690
2- e^- average of configuration	1	1	-135.150496
Closed-shell state 8	2	0	-135.116544

^aClosed-shell MOs $(1a_1^i)^2 \dots (18a_1^i)^2, (1a_2^i)^2 \dots (7a_2^i)^2, (1a_3^i)^2 \dots (15a_3^i)^2, (1e^i)^4 \dots (25e^i)^4, (1e^i)^4 \dots (19e^i)^4, (1a_1^i)^2 \dots (6a_1^i)^2$.

quadrupole and second moments of charge for the entire fragment. Of these, the calculated electric field gradients and quadrupole moments for the low-lying states reported in Table I are shown in Figure 2.

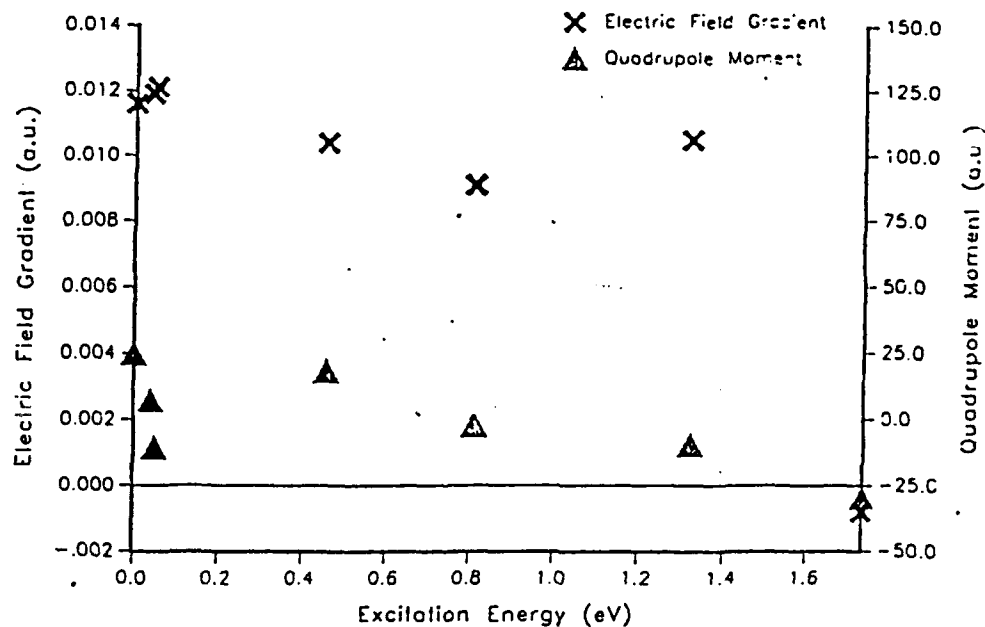


Figure 2. Calculated electric field gradients and quadrupole moments for low-lying states of Be_{133} within 1.75 eV of the ground state as reported in Table I. Properties calculated for states 5 and 6 are superimposed.

Mulliken population analyses [14] were also carried out for the low-lying states reported in Table I. Net charges and gross atomic *s* and *p* orbital populations were calculated for each symmetry-distinct group of atoms. The average net charges from the analyses for the symmetry-distinct groups of atoms are shown in Figure 3.

Valence electronic density distribution maps have also been calculated for the ground state. Contour levels were calculated starting at 6.25×10^{-5} electrons/a.u.³ and doubled thereafter to a maximum of 65.536 electrons/a.u.³. The density distribution maps are shown in Figure 4.

A density of states (dos) analysis was also carried out for the ground state and is shown in Figure 5 [15]. To obtain the density of states, a point corresponding to the number of states in a given orbital energy increment was plotted in the center of the associated increment. The dos was then drawn directly, connecting the plotted points as shown in Figure 5. It was decided not to fit the curves in order to avoid introducing artifacts.

The one-electron energies for the occupied orbitals in the dos were obtained from the ground state wave function while two sets of energies have been plotted for the virtual space. One set of energies corresponds to that obtained from the canonical Hartree-Fock (HF) orbitals while a second set has been obtained from

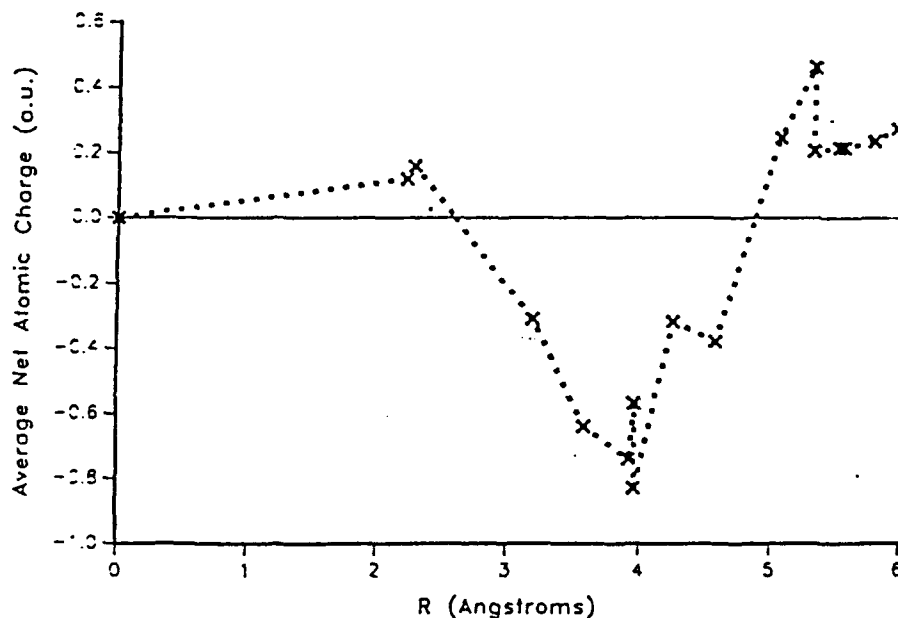


Figure 3. Average net atomic charges for the 20 symmetry equivalent groups of atoms as a function of the radii of the coordination shells [4] containing the respective groups. Sharp corners are artifacts of the relation of groups with the shell structure. Vertical segments are due to groups of atoms that are symmetry equivalent in the bulk but non-equivalent in the fragment.

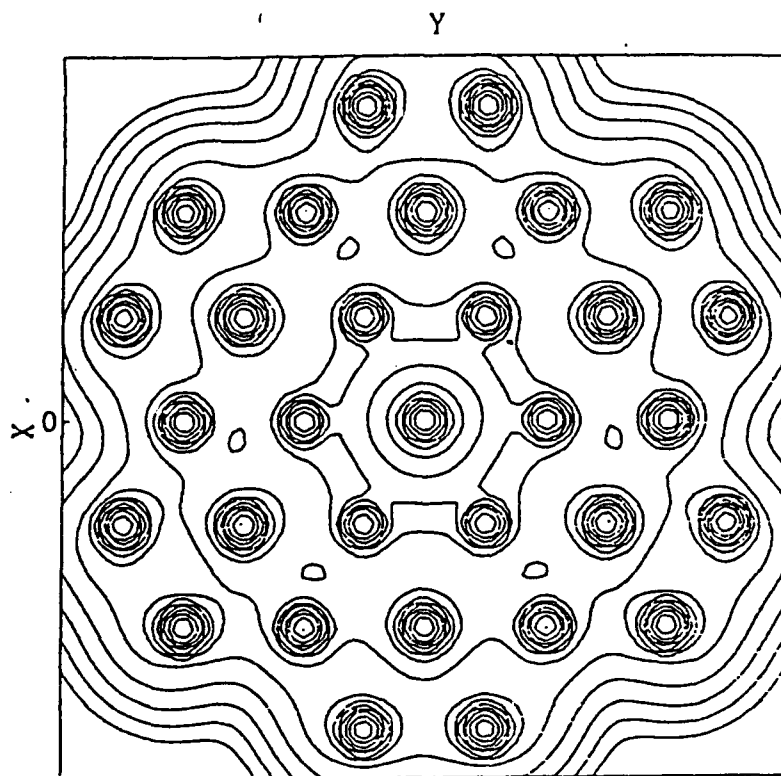


Figure 4. Contours of the molecular valence charge density in the coordinate planes for Be_{135} . Contour levels begin at $6.25 \times 10^{-3} \text{ e}/(\text{a.u.})^3$ and are doubled for each new contour. (a) XY plane, (b) XZ plane, (c) YZ plane.

an improved virtual orbital calculation [16,17]. This was required because the Hartree-Fock unoccupied mos represent the system under study plus one additional electron, i.e., the negative ion [18]. Improved virtual orbitals (ivo) that have been corrected so that they are consistent with the corresponding neutral system were obtained by performing a single iteration self-consistent field (scf) calculation on the ionized fragment with the neutral ground state scf wave function as input. In order to obtain an overall average effect, an appropriate fraction of the ionized electron was removed from each of the highest-occupied molecular orbitals of the irreducible representations of the D_{3h} point group.

In order to determine the optimal energy increment, density of states analyses resulting from use of energy increments of 0.01, 0.035, 0.050, 0.065, 0.080, 0.095, 0.11, 0.135, 0.150, and 0.175 a.u. were examined (at the extreme limits in a dos analysis, the smallest energy increment has a small number or zero states while the largest contains the full set of states). It was found that an energy increment of 0.035 a.u. contains the most dos data points while still maintaining the general features of the curves.

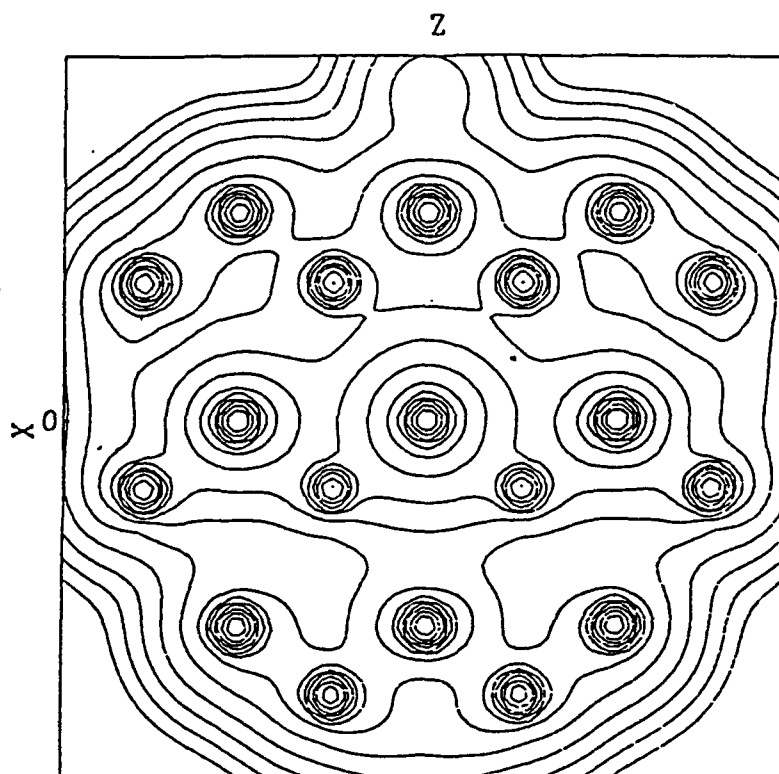


Figure 4. (Continued)

Discussion

As can be seen in Table I, of the 9 states converged to 10^{-9} a.u. in one- and two-electron energy in the HFR studies, 3 are closed-shell states, 5 are open-shell average-of-configuration states, and 1 is a triplet state. In addition to these 9 states, 31 additional states, converged to 0.1 a.u., were found within 4 eV of the ground state. The additional states were not converged further because examination of properties and populations analyses indicated little change from those of the 9 states already studied in detail (Table I).

The results of the present study are consistent with results of earlier fragment studies of greater than 50 beryllium atoms in that calculated properties, populations, and other quantities are largely insensitive to spin coupling for a given electron configuration [2]. For example, as can be seen in Table I, the calculated ionization potential for the triplet state is 3.48 eV and the corresponding average-of-configuration ionization potential is 3.47 eV. Population and properties analyses yield similar comparisons. For example, the electric field gradient at the central beryllium atom is calculated to be 0.0091 a.u. for both states and the quadrupole moments for the entire fragment are calculated to be 18.18 and 18.21 a.u. for the triplet and average-of-configuration states, respectively. In regard to population analyses, the calculated net charges with respect to the

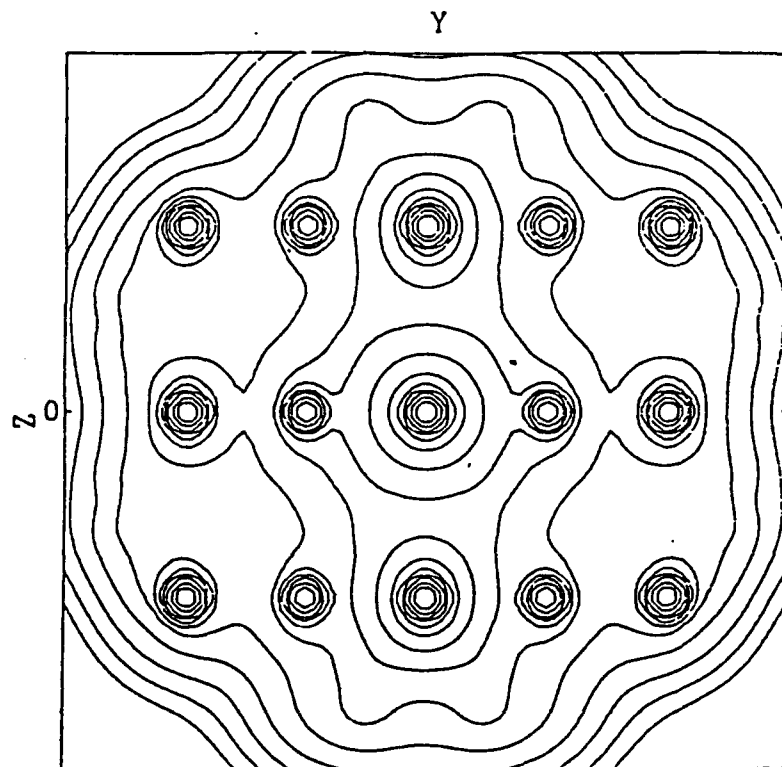


Figure 4. (Continued)

symmetry-distinct groups of atoms have been found to be identical for the triplet and average-of-configuration states.

Calculated ionization potentials at the SCF level (Δ_{SCF}) for the four lowest states, shown in Table I, are all larger than, but within 10% of, the experimental bulk work function [19]. The Koopmans' theorem ionization potential for the lowest state is 0.24 eV larger than the corresponding Δ_{SCF} ionization potential and is 15% larger than the experimental value.

The calculated binding energy per atom for the ground state is 31.7 kcal/mol. In comparing to calculated binding energies per atom for the lowest states of bulk fragments of 51, 57, 69, 81, and 87 atoms, the onset of convergence to the bulk HFR limit employing this basis set is observed. Calculated binding energies for the lowest lying states of bulk fragments of 51, 57, 69, 81, and 87 atoms are 25.8 [2], 25.4 [2], 28.2 [4], 28.3 [5], and 28.5 [5] kcal/mol, respectively. These calculated values yield an incremental increase of 0.077 kcal/mol per atom as the number of atoms is increased from 51 to 87. This can be compared to a smaller incremental increase of 0.066 kcal/mol per atom as the number of atoms is increased from 87 to 135. If the size of the incremental increase is taken to decrease by at least 0.01 kcal/mol per atom for every 42 atom increase in fragment size, an estimate of the maximum contribution to binding energy from further fragment size increase is about 7 kcal/mol per atom.

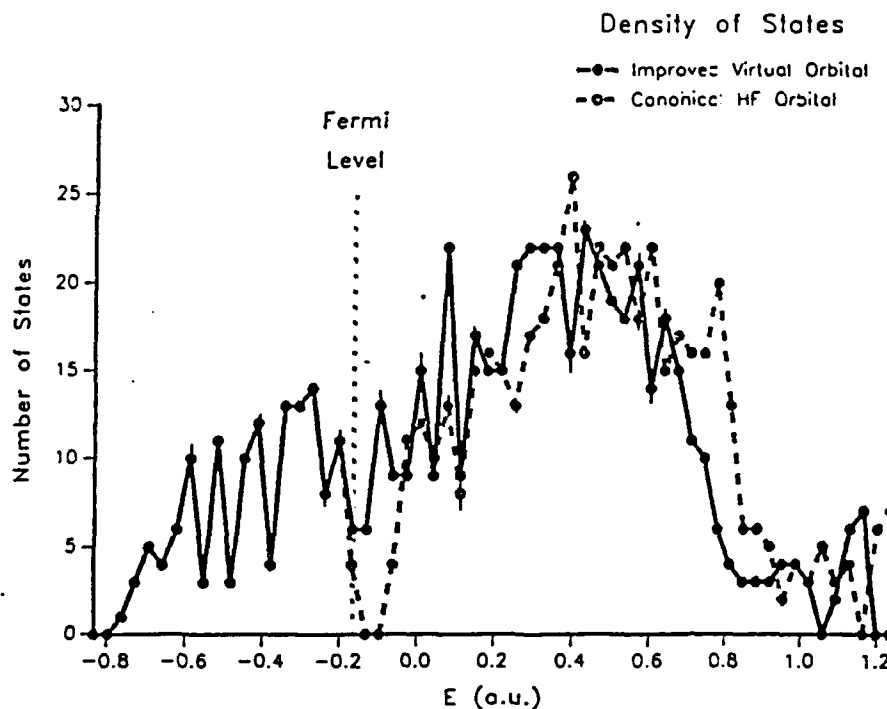


Figure 5. Density of states (dos) analyses for the ground state of Be_{135} for an energy increment of 0.035 a.u.

An estimate of basis set effects on binding energy can be obtained from earlier studies on smaller beryllium fragments and clusters. The effect of uncontracting the current p basis set can be obtained by comparing earlier fragment studies on Be_{51} and Be_{57} [2] to studies by Pettersson and Bauschlicher on Be_{55} [6] and is estimated to increase the binding energy by about 3%. Similarly, the effect obtained by adding an additional p primitive basis function is estimated to increase the binding energy by 14% also based on the same studies [6]. Adding yet another p primitive basis function is estimated to increase the binding energy by 4.5% based on comparing studies on Be_{13} and Be_{55} again by Pettersson and Bauschlicher [6]. The effect of adding a d function can be estimated to increase the binding energy by 20% based on an average of effects observed in studies on Be_4 by Marino and Ermler [20] and Bauschlicher, Bagus, and Cox [21]. Summing these effects for the ground state of Be_{135} , a maximum basis set error of 13 kcal/mol per atom is obtained. It is likely, however, that this estimate is too large based on an observed decrease of 55% in the basis set effect obtained by adding a primitive p function to the basis set in comparing clusters of 13 and 56 atoms [6].

We attribute the remaining 24 to 30 kcal/mol per atom required to attain the experimental binding energy [22] to differential electron correlation energy. This is supported by correlation effects seen in studies on Be_4 of as large as 76 and 54% by Marino and Ermler [20] and Bauschlicher, Bagus, and Cox [21], respectively.

To investigate the mixing between low-lying states, an MCSCF study was carried out for the two lowest closed-shell states. As shown in Table II, these states correspond to the ground state and that obtained by a double excitation from the $8a_1'$ orbital of this state into the unoccupied $18a_1'$ orbital. The total energy for the MCSCF wave function, configuration interaction coefficients, HFR total energies for the two closed-shell states, and the triplet and average-of-configuration states obtained from a single excitation involving the same orbitals are shown in Table II. As can be seen from the configuration interaction (ci) coefficients, there is very little mixing of the two states. This is no doubt due to the small size of the exchange integral between these two orbitals both of which are spread out over the entire cluster. Accordingly, the energy lowering in the MCSCF study is only 0.0048 eV relative to the ground state, indicating that a more extensive correlation treatment is necessary to recover significant correlation effects, as expected.

The calculated average values of the nuclear-electrostatic potential [23] and diamagnetic shielding constant [23] are -1.06 and -33.10 a.u., respectively. For both properties, only one state deviated more than 0.01 a.u. from the average. Consistent with properties computed for fragments of bulk beryllium larger than 51 atoms [2-5], the computed values are relatively constant with electronic state. This behavior is also observed in the calculated values of the square roots of second moments of charge [23], $\langle x^2 \rangle^{1/2}$ and $\langle z^2 \rangle^{1/2}$, which are found to have average values of 93.28 and 88.01 a.u., respectively, and maximum state-to-state variations of 0.19 and 0.24 a.u., respectively. As discussed in the earlier studies, this can be interpreted as a sign of bulk behavior in that smaller fragments exhibit larger changes in properties with electronic state.

The calculated values of the electric field gradient [23] at the central atom and the quadrupole moment [23] for the entire fragment for the lowest eight converged states are shown in Figure 2 as a function of excitation energy. As discussed above, the calculated values for the electric field gradient and the quadrupole moment for states 5 and 6 (triplet and average of configuration for the same molecular orbital occupation) are identical or close to identical for the number of significant figures reported. This results in the points for these states in the figure being superimposed. Calculated values for the highest excited state were not included because no states were characterized between it (at 3.96 eV) and the next lowest state (at 1.74 eV). As mentioned above, the highest excited state characterized was the initial converged reference, which provided an initial wave function to use in probing for lower-lying states. The focus of further characterization was to survey and characterize the region lying between 0 and 1.75 eV of the ground state as shown in Figure 2.

As can be seen in Figure 2, the calculated values of the electric field gradient at the central atom in the fragment range from -0.0008 to 0.0153 a.u. If only the ground state and the six states within 1.5 eV of the ground state are considered, the range is considerably smaller (0.0091 to 0.0121 a.u.). These state-to-state variations in Be_{135} can be compared to state-to-state variations of 0.0159 to 0.0211 a.u., -0.0165 to 0.0163 a.u., and -0.0329 to 0.0526 a.u. for fragments of 69 [4], 81 [5], and 87 [5] atoms. The experimentally observed range of values is

(± 0.0044 – 0.0049 a.u. [22]). Since a significant trend toward the experimentally observed values is not found as the size of the fragment increases from 69 to 135 atoms and since the value of q is so small for beryllium, refinements to the present treatment may be required for highly accurate calculation of this quantity. Such refinements may include increasing the number of atoms, including electron correlation effects, extending the basis set on the central atom, employing an all-electron treatment on the central atom, and investigating the effects of geometry optimization and surface states.

An additional consideration for accurate calculations of the electric field gradient as discussed in an earlier study of a cluster of 63 beryllium atoms [3] is a correction for the Sternheimer effect [1]. The Sternheimer effect takes into account polarization of the core (1s) electrons of the Be atom. This effect results in a 16–18% increase in magnitude in the electric field gradient which, although in the wrong direction in the present case, does not qualitatively alter the agreement with experiment.

As can also be seen in Figure 2, the quadrupole moment [23] is clearly more sensitive to electron configuration since the principal contributions come from the outer orbitals. This is due in part to the definition of the quadrupole moment as a difference of second moments. This effect can be seen by comparing the state-to-state variations of the quadrupole moment in the figure to those observed for the nuclear-electrostatic potential, the diamagnetic shielding constant, and the square roots of second moments of charge discussed above. This effect is also consistent with results from studies on smaller fragments [2–5].

Mulliken population analyses [14] have been carried out on the symmetry-distinct groups of atoms for the low-lying states reported in Table I. The maximum state-to-state variations for the net charges were found to be less than 0.05 electrons for all but 4 of the 20 symmetry-distinct groups of atoms [4]. In the remaining 4 groups of atoms, the maximum state-to-state variation was 0.1 electrons. The small state-to-state variations are consistent with the earlier studies on bulk fragments ranging from 51 to 87 atoms [2, 4, 5] and are indicative of bulk behavior in that the relative populations of the symmetry-distinct sets of atoms are essentially independent of electronic state.

The averages of net charges from the Mulliken population analyses calculated for the low-lying converged states are shown in Figure 3 for the 20 symmetry-distinct groups of atoms as function of the radii of the coordination shells containing the respective groups [4]. As can be seen in the figure, the net charge approaches zero at the center of the cluster, which is as expected in the neutral bulk environment. The average net charges on the central Be atom for bulk fragments of 51, 57, 69, 81, 87, and 135 atoms are 0.32, 0.40, 0.28, 0.15, 0.16, and 0.0 electrons, respectively, indicating a convergence of this quantity to the bulk value in a fragment of 135 atoms.

Figure 3 also shows a buildup of positive charge in the outer region of the fragment complemented by a depletion in the region between the outer and central regions. This may be interpreted as a surface effect in that electrons are being drawn from the surface to the middle region of the fragment so as to be in a region with more positive charge. It may also be an indication that given geometric flexibility, the surface might reconstruct to minimize charge separation.

In addition to net charges on the symmetry-distinct sets of atoms, gross atomic orbital populations were also computed. On the central Be atom, the average values of the s and p gross atomic orbital populations were found to be 0.56 and 1.45 electrons, respectively. The ratio of $p:s$ gross atomic orbital populations is consistent with the valence electron density analysis obtained from X-ray diffraction studies [24], which have been interpreted to indicate sp^3 hybrid bonding in beryllium metal.

The molecular valence charge densities in the XY (perpendicular to the principal C_3 axis of symmetry), XZ , and YZ planes for the ground state of the fragment are shown in Figure 4. The plots display the homogeneity of the charge distribution around the central Be atom when compared to charge densities calculated for fragments of 81 and 87 atoms [5], thus indicating the onset of a constant charge distribution around the central Be in clusters as small as 80 atoms.

Evidence of p participation in the bonding as indicated by the population analyses and X-ray diffraction studies [24] can also be seen in Figure 4 by examining the anisotropy of the bonding in the XZ and YZ planes [Figs. 4(b) and 4(c), respectively]. The noncircular shaped contours are indicative of participation of p orbitals in the interatomic interactions.

Evidence of electronic charge density maxima in regions between nuclei can be seen in Figure 4(a) in the XY plane. These maxima, however, are not in the proper location in the fragment to correspond to the electron density maxima predicted to be located near tetrahedral hole sites in the hexagonal closed-pack lattice by electron density deformation and valence charge density plots from an X-ray diffraction study [24] and a Hartree-Fock band theory study [7]. The current studies are consistent with local density functional band theory (LDFB) studies [9, 10], which also do not predict density maxima at the tetrahedral hole sites.

The density of states (DOS) for the ground state of the fragment can be seen in Figure 5. We find that the DOS for the canonical Hartree-Fock orbitals is zero at an energy immediately following the Fermi level. This is consistent with an earlier study by Monkhorst showing that the DOS at the Fermi level is zero in canonical crystal Hartree-Fock studies on partially filled band systems [25]. It is also consistent with a HF DOS study by Cox and Bauschlicher on Al_{19} in which a gap in the DOS appeared near the Fermi level [26]. In the present study the DOS using canonical virtual orbitals is zero just above the Fermi level since the Fermi level is taken as the energy of the highest occupied state. In contrast, the DOS employing the IVO orbitals is nonzero in the Fermi level region, consistent with the fact that beryllium is a conductor.

The general features observed in the IVO DOS are a dip near the Fermi level, a maximum in the occupied region between -0.25 and -0.30 a.u., and a rapid rise in the unoccupied region leading to a broad maximum starting at 0.35 a.u. These general features indicate a rapid decrease of states in the energy region before the Fermi level followed by a rapid increase in unoccupied states. These features were found consistently in DOS generated using a range of energy increments from 0.035 to 0.080 a.u.

The density of states is not a direct experimentally observable quantity, but interpretation of photo-electron and X-ray emission and absorption spectra can provide insight into the DOS [27]. Detailed comparisons between the IVO DOS and

experiment must take into account other factors such as intensity matrix elements, final-state relaxation effects, and electron correlation. Notwithstanding those considerations, X-ray emission and absorption studies in the present case show evidence of a dip near the Fermi level [28], a rapid rise in unoccupied states [28], and fine structure in the occupied DOS toward the low end of the energy range [29]. These features are consistent with the current IVO DOS and previous DOS analyses calculated for beryllium by Hartree-Fock band (HFB) [7], local density functional band (LDFB) [8,9], and orthogonalized plane wave (OPW) [10] methods. The dip near the Fermi level is also consistent with an additional earlier OPW study by Herring and Hill [11].

As can be seen in Figure 5, the bandwidth of the occupied region of the DOS is 0.61 a.u. This can be compared to a bandwidth of 0.7 a.u. estimated from the DOS in the HFB study [7]. The experimental bandwidth as estimated from experimental X-ray emission spectra is 0.46 a.u. [30]. The larger theoretical bandwidth is consistent with earlier Hartree-Fock studies and has been shown to decrease when electron correlation effects are included [25,26]. Earlier estimates of bandwidths range from 0.39 to 0.45 a.u. depending on whether the LDFB [8,9] or OPW [10,11] model is used.

Conclusions

An ab initio study on a bulk fragment of 135 atoms has been carried out to investigate the electronic structure and density of states in beryllium metal. Convergence to the bulk limit occurs for the net population on the central Be atom. The onset of convergence to the bulk limit is observed for the binding energy per atom. In addition, ionization potentials for the lowest lying states are within 10% of the bulk experimental work function. The density of states employing improved virtual orbitals compares well with experimental evidence. First-principle studies on fragments of this size are shown to give valuable insight into the description of the electronic structure of bulk systems and are in agreement with descriptions obtained both from experiment and from band theory models.

Bibliography

- [1] W. C. Ermler, C. W. Kern, R. M. Pitzer, and N. W. Winter, *J. Chem. Phys.* **84**, 3937 (1986).
- [2] R. B. Ross, W. C. Ermler, R. M. Pitzer, and C. W. Kern, *Chem. Phys. Lett.* **134**, 115 (1987).
- [3] W. C. Ermler, R. B. Ross, C. W. Kern, R. M. Pitzer, and N. W. Winter, *J. Phys. Chem.* **92**, 3042 (1988).
- [4] R. B. Ross, C. W. Kern, R. M. Pitzer, W. C. Ermler, and N. W. Winter, *J. Phys. Chem.* **94**, 7771 (1990).
- [5] R. B. Ross, W. C. Ermler, V. Luana, R. M. Pitzer, and C. W. Kern, *Int. J. Quantum Chem.: Quantum Chem. Symp.* **24**, 225 (1990).
- [6] L. G. M. Pettersson and C. W. Bauschlicher, *Chem. Phys. Lett.* **130**, 111 (1986).
- [7] R. Dovesi, C. Pisani, F. Ricca, and C. Roetti, *Phys. Rev. B* **25**, 3731 (1982).
- [8] P. Blaha and K. Schwartz, *J. Phys. F* **17**, 899 (1987).
- [9] M. Y. Chou, P. K. Lam, and M. L. Cohen, *Phys. Rev. B* **28**, 4179 (1983).
- [10] T. L. Loucks and P. H. Cutler, *Phys. Rev.* **133**, A819 (1964).
- [11] C. Herring and A. G. Hill, *Phys. Rev.* **86**, 132 (1940).

- [12] J. C. Slater, *Quantum Theory of Atomic Structure*, Vol. 1 (McGraw-Hill, New York, 1960), p. 322.
- [13] J. Almlof, K. Faegri, and K. Korsell, *J. Comput. Chem.* **3**, 385 (1982).
- [14] R. S. Mulliken, *J. Chem. Phys.* **23**, 1833 (1955).
- [15] S. M. Sung, B.S. Thesis, The Ohio State University, 1988.
- [16] S. Gayen, W. C. Ermler, and C. J. Sandroff, *J. Chem. Phys.* **94**, 729 (1991).
- [17] W. J. Hunt and W. A. Goddard, *Chem. Phys. Lett.* **3**, 414 (1969).
- [18] C. C. J. Roothaan, *Rev. Mod. Phys.* **23**, 69 (1951); **32**, 179 (1960).
- [19] G. S. Tompa, M. Seidl, W. C. Ermler, and W. E. Carr, *Surf. Sci.* **L453**, 185 (1987).
- [20] M. M. Marino and W. C. Ermler, *J. Chem. Phys.* **86**, 6283 (1987).
- [21] C. W. Bauschlicher, P. S. Bagus, and B. N. Cox, 4032 (1982).
- [22] P. Blaha and K. Schwartz, *J. Phys. F* **17**, 899 (1987).
- [23] D. Neumann and J. W. Moskowitz, *J. Chem. Phys.* **49**, 2056 (1968).
- [24] F. K. Larsen and N. K. Hansen, *Acta Cryst.* **B40**, 169 (1984).
- [25] H. J. Monkhorst, *Phys. Rev. B* **20**, 1504 (1979).
- [26] B. N. Cox and C. W. Bauschlicher, *Surf. Sci.* **115**, 15 (1982).
- [27] D. R. Salahub, *NATO ASI Series E*, J. Davenas and P. M. Rabette, Eds. (Martinus Nijhoff, Boston, 1986), p. 176.
- [28] R. W. Johnston and D. H. Tomboulion, *Phys. Rev.* **94**, 1585 (1954).
- [29] P. Fisher, R. S. Crisp, and S. E. Williams, *Opt. Acta* **5**, 31 (1958).
- [30] H. W. B. Skinner and H. M. O'Bryan, *Trans. Roy. Soc. (London)* **239**, 95 (1940).

Received May 21, 1991

Accepted for publication June 10, 1991.

Spin-Orbit CI Study of Valence and Rydberg States of LiBe

M. M. Marino and W. C. Ermler

Department of Chemistry

The Ohio State University

Columbus, Ohio 43210

and

Molecular Science Research Center

Pacific Northwest Laboratory

Richland, Washington 99352

C. W. Kern and V. E. Bondybey

Department of Chemistry

The Ohio State University

Columbus, Ohio 43210

Abstract

Ab initio spin-orbit full configuration interaction calculations in the context of relativistic effective core potentials are reported for the weakly bound metal dimer LiBe, a 3-valence-electron system. The effects of basis set on the energies of valence and Rydberg states of the cluster are discussed, as are the effects of configuration space selection on the energy of the latter states. Results at the dissociative limit are compared to the experimental atomic spectra. Potential energy curves and spectroscopic constants are presented for the ground state and fourteen excited states, which includes the Li and Be 2p valence states, the Li 3s, 3p, 3d and 4s Rydberg states, as well as three low-lying states of the molecular cation.

I. Introduction

There is great current interest in the structure and chemical properties of small metal clusters.^{1,2} The reasons for the increased research activity in this area are several-fold. First, recent advances in the generation of these species, particularly by laser vaporization techniques, have made it feasible to study them experimentally.³ At the same time, the development of new theoretical methods, combined with the latest advances in computing technology, have made possible the treatment of all types of metal clusters, including those containing heavy elements, at a post-Hartree-Fock level of theory.⁴⁻⁶ Such parallel advances in experiment and theory provide an ideal setting for characterizing these systems.

An accurate theoretical study, however, requires the availability of computational methods which are sophisticated enough to generate reliable electronic spectra, potential energy curves and wave functions while still remaining tractable. One of the most powerful general methods to date is full configuration interaction (full CI). It is, however, computationally demanding and, depending on the number of electrons, impossible to perform on heavy elemental clusters because of the large number of terms which must be stored and manipulated. The method employed in this study replaces the core electrons of each atom with averaged relativistic effective potentials (AREP's),⁶ thus reducing the electrons in the valence region to a number small enough such that a full CI treatment is feasible. In this case, the only errors introduced arise from the AREP's and the finite basis set. If the AREP's used are determined to be accurate, then the error is attributable almost solely to inadequacies in the basis set. It is then possible to determine the most appropriate basis set for the accurate calculation of the electronic spectra of the system.

This paper reports the effects of basis set changes on the electronic energies of the valence and Rydberg states of LiBe using a full CI treatment that incorporates the spin-orbit operator explicitly in the Hamiltonian (SOC). The incorporation of a spin-orbit operator increases the accuracy of the calculated results.⁷ The core electrons of both Li and Be are represented by AREP's, thereby reducing the number of electrons in the valence region to exactly three. Potential energy curves and spectroscopic constants for the ground and several excited states of LiBe and LiBe⁺ are presented, and, where possible, the results are compared with experiment.

II. Calculations

The SOCI procedure involves a Hamiltonian matrix that is constructed in terms of elements involving, in addition to the terms in the nonrelativistic Hamiltonian operator for the valence electrons, averaged relativistic effective potentials (AREP), a spin-orbit hamiltonian H^{SO} and determinantal wavefunctions for valence electrons defined through standard L-S coupling SCF procedures.^{8,9} The REP's are defined using shape-consistent nodeless pseudo-orbitals¹⁰ extracted from numerical two-component Dirac-Fock atomic spinors¹¹ using the procedure of Lee et al.¹² The pseudo-orbitals are derived such that nodes in the respective atomic spinors are removed by requiring that up to five derivatives be matched at a distance from the atomic nucleus beyond which the nodeless orbital is exactly the same as the true Dirac-Fock solution.¹⁰ Such pseudo-orbitals are then used to define individual REPs in j-j coupling. The $j \pm \frac{1}{2}$ components are then used to form weighted average REP (AREP) operators and spin-orbit (SO) operators.^{6,7} Because the SOCI calculations result in wavefunctions that transform according to one of the irreducible representations of the C_{2v} ' double group, and since LiBe possesses an odd number of electrons, all possible states are extracted from a single Hamiltonian matrix of E symmetry.⁹ This is a clear advantage in the full CI procedure in that energies and wavefunctions of all electronic states for a given internuclear separation can be extracted as successive eigensolutions of one matrix provided the atomic basis sets are adequate.

The AREP's used in this work describe the 1s electrons of both Li and Be.¹³ Basis sets of contracted Gaussian functions were optimized at the atomic level and used to describe the valence states of both atoms. These sets are given in Table I. In the case of Li, one diffuse Gaussian function was included initially in the basis to describe the Rydberg 3s and 4s states. The basis functions for the Li 3p and 3d Rydberg states, as well as improved basis functions for the Li 3s and 4s Rydberg states, were composed of Gaussian expansions of Slater-type orbitals (STO-6G).¹⁴ The exponents of the latter functions were scaled to describe the corresponding orbitals of the Li atom. The scaling parameter was determined¹⁵ from the quantum defect using experimental ionization potentials and the corresponding atomic energies of the Rydberg states of the Li atom. For each Rydberg orbital, $\zeta = 1/n^*$, where ζ is the exponent for the Slater orbital representing a given Rydberg state, $n^* = n - \delta$ and δ is the quantum defect of the orbital of principal quantum number n . Here, $n^* = [R/(\Delta E_{ion} - \Delta E_R)]^{1/2}$ and ΔE_{ion} and ΔE_R are, respectively, the experimental atomic ionization and excitation energies

corresponding to a particular Rydberg state.¹⁶ R is the Rydberg constant. ($R = 109734 \text{ cm}^{-1}$). Given the experimental energies, it is possible to calculate ζ for each Rydberg orbital. Exponents α for such values of ζ are obtained from those for $\zeta=1$ by multiplying each α in the Gaussian expansion of Slater-type orbitals by ζ^2 .¹⁴ The exponents and coefficients of the resulting Rydberg STO-6G functions are given in Table II.

Energies corresponding to internuclear separations from 3.5 to 10 bohr were calculated for the ground, excited valence and ionic states. The calculated energies of the Rydberg states correspond to internuclear distances from 3.5 to 7 bohr; specifically, 3.5, 3.95, 4.5, 4.896, 5.5, 5.85, 6.5, and 7.0. The energies corresponding to distances greater than 7 and up to 10 bohr for these states were derived from a fit to a Hulbert-Hirshfelder (H-H) analytical form.¹⁷ The energies of all the states of the neutral and cationic systems were also calculated for an internuclear distance of 40 bohr. In addition, calculations were completed for $R=10^6$ bohr for the cation. Spectroscopic constants for the ground, excited valence, Rydberg and ionic states were calculated to second order of perturbation theory by fitting the energies of each to a high-degree (6th or higher) Taylor series.

In certain cases a selection scheme was used to obtain the spatial configurations comprised of double-group symmetry-adapted MO's that were retained in the SOCI wavefunction. Two cases were treated to determine the effects of such configuration selection on the energies of the Rydberg and valence states of the system. The first involved inclusion of the complete set of valence configurations plus all Rydberg configurations. The second case included all valence and Rydberg configurations as well as all configurations corresponding to single excitations relative to the Rydberg configurations. In each instance, the CI wavefunction was calculated using configurations derived from the $1\sigma^2 2\sigma$ SCF MO's of the LiBe ground state plus orthonormal virtual (unoccupied) MO's, and the results were compared to the corresponding full SOCI values.

The dissociative limit was assumed to be 40 bohr, at which point the resulting theoretical values were compared to atomic spectra.¹⁶ All calculations were performed on a Cray Y-MP supercomputer using codes that are part of the COLUMBUS suite of programs.^{9,18} The calculations involving the largest basis set (56 basis functions) required approximately 25 hours of cpu time to construct and extract as many as 50 roots of the Hamiltonian matrix comprised of 30,800 double group symmetry adapted configurations and 113,960 determinantal wave functions. The Hamiltonian matrix required approximately 0.75 gigabytes of disk storage.

III. Results and Discussion

A. Electronic Spectrum

The theoretical spectrum of LiBe at dissociation, including the 3s, 3p, 3d and 4s Rydberg states of Li, each represented by an STO-6G function (basis set 6 in Table I), is given in Table III. State 1 of Table III is the ground state, states 2 through 4 correspond to the Li 2p (2P) states, while states 5 through 13 correspond to the Be 2p (3P) states. The Li Rydberg 3s, 3p, 3d and 4s states are 14, 15 through 17, 18 through 22 and state 23, respectively. Although not shown in Table III there are a total of 27 additional states that correspond to double excitation states of the LiBe system. Simultaneous single excitations of both Li and Be electrons give rise to these states, which lie at approximately 4.61 eV and have energies that are sums of the single excitation energies of Li and Be. Also shown are low-lying states of LiBe^+ . The 1st and 11th of these are the ionization potentials of Li and Be, respectively, while the 2nd through 10th correspond to the ionization of Li plus the Be 2s2p (3P) excitation. All of the calculated values are in excellent agreement with experiment, the largest error being 0.05 eV for both the 3d states and ionization potential of Li.

The potential energy curves for LiBe were calculated using basis set 6. Figure 1 shows the curves calculated for the ground, valence and cation states and their corresponding atomic states at dissociation. The three highest-lying curves shown correspond to the three lowest states of LiBe^+ . The dissociative limit of the first of these is $\text{Li}^+ + \text{Be}$. The second and third correspond to dissociation to $\text{Li}^+ + \text{Be}(^3P)$. The states lying between -1.13 and -1.06 hartrees are shown on an expanded scale in Figure 2.

Calculated atomic spin-orbit splittings are in excellent agreement with experimental values¹⁶ for both the neutral and ionic systems. The greatest discrepancy is 0.1 meV (Table III). The largest spin-orbit splitting calculated is 0.2 meV between both the neutral $^2S + ^3P_1$ and $^2S + ^3P_2$ and the ionic $^1S + ^3P_1$ and $^1S + ^3P_2$ states. The experimental splittings are 0.3 meV for each. The rest of the states have splittings in the range 0.0-0.1 meV as both calculated and observed.

The spin-orbit splittings corresponding to the equilibrium internuclear separations are also small. The $A^2\Pi$, $C^2\Pi$, $b^4\Sigma^-$, $^2\Pi(3p)$, $^2\Delta(3d)$ and $^2\Pi(3d)$ states of neutral LiBe are each split into two spin-orbit components. The splittings are 0.08, 0.0, 0.0, 0.008, 0.0 and 0.03 meV, respectively. The $a^4\Pi$ state contains four spin-orbit components. Each is separated by 0.04 meV from the state or states lying closest to it in energy, making the total spin-orbit energy range 0.12 meV. The $B^3\Pi$ state of LiBe^+ is split into three spin-

orbit states. There is a splitting of 0.22 meV between the lowest component and the higher two, which are degenerate.

The equilibrium internuclear separation (R_e), harmonic frequency (ω_e), anharmonicity constant ($\omega_e x_e$), rotational constant (B_e), vibration-rotation coupling constant (α_e), zero-point vibrational energy (G_0), and minimum-to-minimum electronic excitation energy (T_e) for the ground, excited valence, Rydberg and ionic states appear in Table IV. Spectroscopic constants for the ground state are in excellent agreement with those calculated previously using a numerical solution to the nuclear motion Schrodinger equation.¹⁹ Most of the states have similar ω_e values with the exceptions of the $C^2\Pi$, $D^2\Sigma^+$, $A^2\Pi$ and $b^4\Sigma^-$ states. The first two have a low harmonic frequency due to their broad, shallow wells. The latter two have wells that are relatively deep - which accounts for their higher frequencies - and similar in shape and thus have very close values of ω_e . Most of the rotational constants have comparable values (between 0.5 and 0.7 cm^{-1}), as expected, since the equilibrium internuclear separations, R_e values, lie between 5 and 6 bohr. One exception is the $D^2\Sigma^+$ state, whose B_e value is low (0.33 cm^{-1}) compared to the others due to its relatively long equilibrium internuclear separation (6.73 bohr). The other two exceptions are the $A^2\Pi$ and $b^4\Sigma^-$ states whose R_e values are closer to 4 bohr, resulting in larger B_e values. The equilibrium rotation-vibration coupling constants are also similar for all states except the $D^2\Sigma^+$ and $^2\Pi(3d)$, which have negative values of α_e . The latter curve actually starts out at small R as a repulsive state. However, the avoided crossing between it and the $^2\Pi(3p)$ state causes the curve to swing up and thus become more harmonic. The low anharmonicity of the state results in a negative α_e . The former state also has a negative value of α_e . In this case, the $D^2\Sigma^+$ state would have had a much deeper well. However, the avoided crossing between it and the $^2\Sigma^+(3s)$ Rydberg state causes the former curve to swing down, resulting in a long, shallow minimum with a low anharmonicity. Again, all of the states have comparable G_0 values with the exception of the $C^2\Pi$ and $D^2\Sigma^+$ states, which have low G_0 (96 and 85 cm^{-1} , respectively). This is due to the fact that these two states are very broad and shallow. T_e values show that there are two low-lying excited valence states ($A^2\Pi$ and $B^2\Sigma^+$). The rest of the states are more than 10,000 cm^{-1} higher in energy relative to the ground state. It is noted that the $b^4\Sigma^-$ valence state is close in energy to the Rydberg $^2\Sigma^+(3s)$ state, the energy difference being approximately 1000 cm^{-1} . It is therefore possible that the Rydberg and higher valence states interact. This is, in fact, the case between the $D^2\Sigma^+$ and $^2\Sigma^+(3s)$ states, which undergo an avoided crossing. Therefore, an accurate spectral study requires the inclusion of Rydberg functions in the basis set.

Table IV also lists the dissociation energies (D_e) for all of the states calculated.

The ground state of LiBe is bound by 0.25 eV. This is in agreement with previous calculations.¹⁸⁻²¹ The latter reference further points out that the bonding is largely due to van der Waals interactions and substantiates this by showing that the dissociation energy of LiBe is proportional to $1/r_e^6$. The remaining states of both the neutral and ionic systems are weakly bound, with the exceptions of the $A^2\Pi$ and $b^4\Sigma^-$ valence states, which are bound by 1.50 eV and 2.03 eV, respectively, and the valence $4\Sigma^+$ (I) state. The latter involves a repulsive interaction (Figure 2). Despite weak bonding in most cases, all of the excited states for the neutral system, as well as the two lower-lying states of the ion, exhibit more bonding than the ground state. The equilibrium internuclear distances (R_e 's) of all the states spread over a fairly large range, approximately 4.0 - 7.0 bohr.

As shown in Figure 1, the first three states calculated for the neutral system and all three states of the ion are simple, i.e., there are relatively few interactions among these due to the large energy differences involved. Where the curves approach each other, only two crossings - between the X and A states at 3.6 bohr and between the A and B states of LiBe at 6.8 bohr - are calculated. The major area of interaction occurs among the upper valence and Rydberg states. This area is shown on a larger scale in Figure 2. Previous calculations¹⁸ agree very well with those reported here for the valence states. However, that work focussed on the valence states of LiBe and therefore the basis set did not include Rydberg functions. Because of the interactions among the upper valence and the Rydberg states, an accurate representation of the valence states lying higher in energy than the $a^4\Pi$ state could not be made without inclusion of the Rydberg functions to the basis set. Discrepancies between the upper valence curves presented here and those of the previous work are a consequence of the differences in the basis sets used.

As stated previously, the most interesting region in Figure 1 appears on an expanded scale in Figure 2. There are three avoided crossings shown here. The first occurs at approximately 4.8 bohr and is between the $D^2\Sigma^+$ and the Rydberg $2\Sigma^+$ (3s) states. This is the reason for the large anharmonicity seen in the latter ($\omega_e x_e$ is 9.2 cm^{-1}). The second avoided crossing occurs at 7.3 bohr and is between the $2\Sigma^+$ (3d) and $2\Sigma^+$ (4s) states, leading to a higher anharmonicity for these, also. However, since the avoided interaction is farther from the equilibrium internuclear separation for both, their $\omega_e x_e$ values (5.0 and 6.0 cm^{-1} , respectively) are smaller relative to those of the state involved in the previous avoided crossing. The third avoided interaction occurs at approximately 5.8 bohr between states 2Π (3p) and 2Π (3d). Again, $\omega_e x_e$ is large (6.7 cm^{-1}) for the former state due to this interaction. If the crossing were allowed, the latter state would be repulsive. However, as a result of the avoided interaction with the 2Π (3p) state, it curves upward, forming a shallow well with a relatively small $\omega_e x_e$ (3.1 cm^{-1}).

It was mentioned above that the region greater than 7 bohr in Figure 1 and corresponding to the Rydberg states contains energies which were approximated using a H-H analytical form. This function is excellent for a general characterization of each curve, especially in the region between the equilibrium internuclear distance and the dissociative limit. However, the description is expected to be less accurate in cases where the interactions among curves results in a deviation from the usual curve behavior, as in the case of avoided crossings. For most of the curves in Figure 1 this approximation holds very well. For example, the difference between the H-H energy and the calculated energy of the ground state at 8 bohr is 0.2 mhartrees (-1.2057 vs -1.2059, respectively). At 10 bohr it is 0.3 mhartrees (-1.2046 vs -1.2049). In the region corresponding to internuclear separations between 7 and 10 bohr there are five cases where the curves either cross or avoid, and thus five possible areas where the H-H approximation may break down. The lowest-energy of these is the crossing between the $a^4\Pi$ and the repulsive $^4\Sigma^+(I)$ states at approximately 9 bohr. This crossing is predicted by the H-H approximation and verified by calculation. The agreement between the two methods results from the fact that even though the curves cross, the crossing does not alter their shape. The second case involves the $^2\Sigma^+(3p)$ and $^2\Pi(3p)$ states. These curves are calculated to cross at about 7 bohr. After the crossing, the latter swings down but must curve up again since it cannot dissociate to the 3s limit. It is then possible that it may cross the $^2\Sigma^+$ state again or parallel it toward dissociation. The second choice is more probable. This curve cannot dissociate to a 3d asymptote, and the likelihood that it will cross the $^2\Sigma^+$ state again decreases as the dissociative limit is approached. The third case is the crossing between the $^2\Pi(3d)$ and $^2\Delta(3d)$ states at about 7.5 bohr. The avoided crossing between the $^2\Pi(3d)$ and the $^2\Pi(3p)$ states at approximately 6 bohr discussed earlier causes the former curve to swing upward, crossing the $^2\Delta(3d)$ state again. The curve continues upward to cross the $^2\Sigma^+(3d)$ state (the fourth case) before dissociating. The latter crossing occurs because the calculated avoided interaction between the $^2\Sigma^+(3d)$ and $^2\Sigma^+(4s)$ states discussed previously causes the former state to dip down before dissociating. The last area of interest is the avoided crossing between the $^2\Sigma^+(3d)$ and $^2\Sigma^+(4s)$ states. Although the curves actually avoid at about 7.5 bohr, this behavior is easily predicted at approximately 6.5-7 bohr from the slope of the curves and the fact that a crossing between them is forbidden due to symmetry. The behavior of the higher-lying curves is expected to be approximated very accurately by the H-H function because the energy differences among the curves is large enough to ensure no interactions between 7 bohr and dissociation.

This study involved the calculation of 29 states of the LiBe and LiBe⁺ systems.

18 of which appear in Figure 1. The rest are spin-orbit components of the those pictured and are not resolved on the energy scale shown. To date no studies of this magnitude have been published for LiBe. However, an experimental and a theoretical spectrum has been published for LiMg.²² Since Mg is a relatively light element belonging to group IIa, this system is similar to LiBe and therefore the spectrum of one may be compared to that of the other. The first five states calculated for LiMg - $X^2\Sigma^+$, $A^2\Pi$, $B^2\Sigma^+$, $C^2\Pi$ and $D^2\Sigma^+$ - are very similar in shape and relative positions to the corresponding states of LiBe. B_e values for the last two LiMg states listed are 0.4737 and 0.3583 cm^{-1} , respectively, compared to the corresponding values of 0.459 and 0.337 cm^{-1} for LiBe. As in LiBe, the $X^2\Sigma^+$, $C^2\Pi$ and $D^2\Sigma^+$ states are more shallow than the $A^2\Pi$ and $B^2\Sigma^+$. However, our calculations indicate that the $D^2\Sigma^+$ state avoids the higher-lying $^2\Sigma^+(3s)$ Rydberg state, causing a slight shoulder in the former at approximately 5 bohr. Although it is unclear whether a similar interaction occurs in LiMg because the atomic Mg 3P and 1P excitations are lower in energy than the corresponding ones in Be, it is possible that interactions do occur among the lower-lying Rydberg states and the higher-lying valence ones and that these interactions would alter the shape of the reported curves.²²

B. Basis Set Effects

The effects of basis set on the Li Rydberg 3s and 4s states were studied using five different sets, each of which varied in both the number and type of valence and Rydberg functions comprising them. The energy levels computed with these basis sets appear in Table V. All values are in eV and represent energy differences between the ground and excited states. The basis sets are described in Table I.

In all cases, state 1 is the ground state and states 2-4 correspond to Li 2p (2P) excitations. The three nearly degenerate roots observed are a result of the incorporation of spin-orbit effects into the calculation. States 5-13 correspond to Be 2p (3P) excitations. Again, the presence of the spin-orbit operator causes the appearance of nine nearly degenerate roots. State 14 of basis sets 2, 3, 4 and 5 corresponds to the Li 3s Rydberg state, while state 15 of basis set 3 and state 23 of basis set 5 correspond to the Li 4s Rydberg state. The higher-lying states, all occurring at approximately 4.39 eV for the first four basis sets mentioned, correspond to poor representations of higher-lying Rydberg states of LiBe. The energies are slightly improved (from 4.389 to 4.392 eV) as the valence basis set on Li is increased from double to triple zeta and one Li s Rydberg function is added to the basis set. This clearly indicates that basis sets 1 through 4 provide an inaccurate

description of the LiBe electronic spectrum at dissociation. This inadequate description of these states, either by a lack of Li Rydberg functions (basis set 1) or an incomplete set of Rydberg functions (basis sets 2 through 4, which are missing functions that describe the 3p and 3d Rydberg states) causes their energies to appear much higher than they actually are. Because the SOCI calculation is variational, the use of a small basis set results in higher-than-actual energy values. As the basis set is improved, the energy of the states would decrease, thereby approaching their proper values. The appearance of the Li 2S (3s) Rydberg state at 3.8779 eV (basis set 2) does not affect the energies of the remaining states. This also applies to the appearance of both the Li 2S (3s) and 2S (4s) Rydberg states at 3.4179 and 4.3169 eV, respectively (basis set 3). The energies of states 14 through 16 in column 5 (basis set 4) are not affected relative to the energies of the same states in column 4 (basis set 3) despite energy differences of 0.05 and 0.03 eV between the Li 3s and 4s Rydberg states, respectively, in these two columns. In other words, basis set 4 leads to a lowering of 0.05 eV in the energy of state 14 relative to the energy of this state in column 4, which corresponds to basis set 3. However, the energies of states 16 through 18 are only 0.00005 eV higher relative to the energies of these same states in column 3. The lowering of the Rydberg 3s and 4s states of Li to their proper values does not shift the energies of the remaining Rydberg states to their correct values of approximately 3.8 eV. The error in these energies therefore predominantly arises from the absence of Rydberg 3p and 3d functions in the Li basis set. These functions would give rise to the Li 2P (3p) and 2D (3d) states, which occur at 3.8 eV.¹⁶ This is, in fact, the case for basis set 5, which is the most accurate of the basis sets appearing in Table V. This basis set contains one STO-6G function to represent each 3s, 3p, 3d and 4s Rydberg state of Li (see Table I). The resulting energies are in very close agreement to those corresponding to basis set 6 in Table III.

Despite the fact that basis set 1 is small (double zeta quality for the description of both s and p valence states of Li and Be), the energies of the Li 2P and Be 3P valence states are very close to the experimental atomic values, the energy differences being only 0.01 and 0.05 eV, respectively. Expansion of the Li valence basis set from double zeta s (basis sets 1 and 2) to triple zeta s (basis sets 3 and 4) lowers the energy difference between the experimental and theoretical values corresponding to the Li 2P valence states by 0.003 eV. As expected, the energies of states 5 through 13 are not affected by this change since they correspond to Be valence states. The energies of the Li Rydberg states, on the other hand, are too high, a result of absent Li 3p and 3d diffuse functions to describe these states, as mentioned previously. It would appear then that even the smallest basis set used provides an adequate description of the valence space and that

subsequent expansion of the Li basis set to include s, p and d Rydberg functions should yield a theoretical spectrum in good agreement with experiment. However, this is not the case. Basis sets 2 and 3 both contain the exact same diffuse Gaussian function on Li to describe the Rydberg 3s and 4s states. The only difference between these two basis sets lies in the degree to which the Gaussian s-type valence basis functions are contracted. Basis set 2 contains six primitive valence Gaussian s-type functions contracted to two, while basis set 3 contains the same Gaussian s-type valence basis functions contracted to three. This extra degree of freedom in the basis set is the reason that only the 3s Rydberg state appears in the energy spectrum corresponding to basis set 2 whereas both the 3s and 4s Rydberg states appear in the one corresponding to basis set 3. Furthermore, the energy of the Li 3s Rydberg state (state 14) corresponding to basis set 2 is 0.5 eV higher in energy than the experimental value of 3.37 eV.¹⁶ The energy of the Li 3s Rydberg state corresponding to basis set 3 (also state 14), on the other hand, is only 0.04 eV lower than the experimental value. The fact that the energy of this state is closer by a factor of ten to the experimental value using basis set 3 is a surprising result given that both basis sets contain the same Gaussian function to describe the Li 3s and 4s Rydberg states. It is clear then that basis set 2 is too small to provide an accurate representation of the LiBe energy spectrum, despite the apparent accuracy of the resulting Li $2P$ valence state energies. Because of this inadequacy, the diffuse s-type Gaussian function used to represent the Li s Rydberg states is not only describing these states, but it is also contributing to the valence space in the case of basis set 2. The error in the energy of state 14 corresponding to basis set 2 is therefore a result of the 'double duty' performed by this function.

Relaxation of the contraction of the Li s basis from double zeta to triple zeta not only results in the theoretical energy of the Rydberg state being ten times more accurate relative to the experimental value, but it also results in the appearance of the Li 4s Rydberg state, the energy of which is 0.02 eV lower than the experimental value of 4.34 eV.¹⁶ An adequate description of the Rydberg states of the LiBe system is pivotal to the calculation of an accurate electronic spectrum, a fact exemplified by the large errors in the energies of these states resulting from the use of a small basis set. However, the accurate representation of these states is affected not only by the quality of the Rydberg functions incorporated into the basis set, but also by that of the valence basis functions themselves. A good description of the electronic states of the system requires both inclusion of accurate Rydberg functions in the basis set as well as augmentation of the valence basis functions.

Table V shows that the energies of the Li Rydberg 3s and 4s states

corresponding to basis set 4 contain only a 0.005 and 0.01 eV deviation, respectively, from the experimental values.¹⁶ The closer agreement to experiment results from the use of a Slater-type orbital formed from an expansion of six Gaussian orbitals (STO-6G) to describe these Rydberg states as opposed to the single Gaussian orbital contained in basis sets 2 and 3. The calculated spectrum further improves when STO-6G representations of 3p and 3d Rydberg orbitals are added to the basis set (basis set 5).

Although no mention has been made concerning the adequacy of the basis set corresponding to Be, the same conclusions apply. Be does not possess Rydberg states in the energy region appearing in Tables III, V and VI. However, the double excitation states appearing in Table VI are a combination of both Li and Be single excitations, the energies of which are consequently affected by the quality of the Be valence basis set. The fact that the double-zeta Li basis set provides such a poor description of the LiBe system leads indirectly to the conclusion that the Be basis set also needs to be augmented, and Be single excitation states, the energies of which are influenced by the quality of the Be valence basis set, are thereby affected. The effects of basis set on the single excitation states of Be can be seen by comparing the energies of these states (states 5-13) in Tables III and VI. The former table contains energy values calculated using basis set 6 of Table I, while the values appearing in the latter were calculated using basis set 5 of Table I. Augmenting the Be valence basis set from 2s2p1d to 4s3p2d results in a 0.01 eV lowering.

As discussed previously, the Rydberg states are sensitive to the quality of the valence basis set, and, as already observed, it is possible to calculate an electronic spectrum having seemingly accurate energy values for the valence states even with a basis set that is not of good quality. All of the calculations discussed to this point were accomplished at the dissociative limit of 40 bohr. Of course, as the internuclear distance is decreased, the interaction between centers increases. The basis set employed, therefore, must be balanced enough to provide a comparable description of both centers and large enough to allow the flexibility necessary to yield accurate electronic state energies. Basis set 5 does not meet these criteria because it is of triple zeta quality with respect to the Li s valence states but only double zeta with respect to the Be s ones. It was discussed previously that a basis set of double zeta quality is too small to provide an accurate description of the system at the dissociative limit. It is therefore clear that this type of basis set cannot provide an accurate description of the LiBe spectrum at shorter internuclear distances. The fact that the calculation appearing in Table III and the one corresponding to basis set 5 in Table V yield energies in such close agreement to each other and to the atomic experimental values despite the poor quality of the basis set employed underlines the importance of ascertaining that a proper basis set has been

chosen before proceeding with further calculations, especially at internuclear distances near equilibrium. The full spin-orbit procedure used in the present calculations is ideal for this type of study since the only sources of error possible in a full CI calculation of this type arise from either the effective core potentials and/or the basis set. If the accuracy of the core potentials is established, then the main source of error lies in the basis set.

C. Configuration Selection

All of the results reported so far have been calculated using the full spin-orbit CI method. A typical calculation employing the highest quality valence basis set reported here and including one STO-6G orbital for each of the four Rydberg states of Li (3s, 3p, 3d and 4s) required approximately 25 cpu hours of Cray Y-MP time for one internuclear distance. Since the amount of time required to complete a calculation is roughly proportional to the square of the number of determinants (which are, in turn, proportional to the number of orbitals), the size of the basis set is pivotal in determining the tractability of a given full SOCI calculation. For low-lying states of the LiBe system, only the Li center requires the inclusion of Rydberg functions in the basis and for this case, only four Rydberg states lie within the energy range of interest. Extension of the SOCI procedure to systems requiring a larger valence basis set and/or the inclusion of a greater number of Rydberg functions to describe these states for one or both centers may lead to unmanageable calculations at the full CI level. However, the systems may still be treated at this level of theory providing that a set of configurations smaller than that of the full CI may be selected without the introduction of significant error.

Table VI shows results of two configuration selection schemes - CSS1 and CSS2 - used in the SOCI calculations for the LiBe system using the most accurate basis set reported here (basis set 6). For each case, the results are compared to the full SOCI to determine the accuracy of the configuration selection scheme employed. The full SOCI calculations required 9102 double group spatial configurations. CSS1 contains all configurations involving single, double and triple excitations among the valence orbitals and, in addition, only those configurations which correspond to Rydberg states. A total of 4072 configurations were included. Results corresponding to thirteen states are reported. (The higher-lying states are double excitations involving Li and Be valence orbitals.) No Rydberg states appeared using this configuration selection scheme. It is also interesting to note that the number of configurations treated was not flexible enough to lead to a

near triply degenerate set of Li $2P$ states. The spin-orbit splitting between the $2P_{1/2}$ and $2P_{3/2}$ states is overestimated because of imbalance in the number of configurations which contribute to these states. Certain configurations that involve excitations among valence and Rydberg states obviously contribute to the $2P_{3/2}$ states. Since these were not included, the energy of these orbitals was calculated to be higher than the actual values, breaking the degeneracy.

CSS2 included all of the configurations of CSS1, as well as all single excitations with respect to each Rydberg configuration, resulting in a total of 7407 configurations. The results agree closely with those of the full SOCI, the largest error being 0.00004 eV. In this case, the Li $2P_{1/2}$ and $2P_{3/2}$ valence states were calculated to be nearly degenerate. It is therefore apparent that the Rydberg states of the Li atom treated in this work are truly SCF-like. The radial extent of these Rydberg orbitals is such that an electron occupying them essentially 'sees' a positive ion core, i.e., occupation of these orbitals results in a hydrogenic system. Inclusion of all configurations involving single excitations with respect to the Rydberg states is therefore needed to allow for ion core molecular orbital relaxation effects that arise from the hydrogenic behavior, since any configuration space smaller than the full CI results in the wave function being dependent on the precise forms of the orbitals. Selectively reducing the configurations in the SOCI from 9102 to 7407 resulted in a savings of approximately twenty minutes of Cray Y-MP cpu time. However, since the time required to complete a calculation scales as the square of the number of determinants generated, the savings will prove to be significant for a system containing a large number of Rydberg states.

Summary and Conclusions

Ab initio spin-orbit full SOCI calculations on LiBe in the context of relativistic effective core potentials predict that the system is weakly bound, with a dissociation energy of 0.25 eV corresponding to an equilibrium internuclear separation of 4.95 bohr. A total of 29 states were calculated - 25 for the neutral system and 4 for LiBe⁺. Of these, eighteen appear in Figure 1, while twelve were spin-orbit components of those already plotted and thus are not resolved on the energy scale shown. The calculated energies of all the atomic states are in excellent agreement with experiment, the largest error being 0.05 eV for both the neutral $2D + 1S$ and ionic $1S + 1S$ states. All of the excited states of neutral LiBe exhibit more bonding than the ground state. The energy range is 0.30-2.03 eV and their equilibrium internuclear separations range from 4-7 bohr.

The calculated atomic spin-orbit splittings are in excellent agreement with experiment for both the neutral and ionic systems, the largest error being 0.1 meV. The largest splitting occurred between the neutral $^2S + ^3P_1$ and $^2S + ^3P_2$ and the ionic $^1S + ^3P_1$ and $^1S + ^3P_2$ states. The rest of the atomic states exhibit spin-orbit splittings in the range 0.0-0.1 meV. Molecular spin-orbit splittings for the neutral system range from 0.0-0.08 meV, with the largest splitting occurring between the components of the $A^2\Pi$ state. The largest splitting is 0.22 meV between the components of the $B^3\Pi$ state of the cation.

The lower-lying Rydberg and upper-lying valence states were found to interact and affect the shape of the reported curves. It was therefore necessary to include Rydberg functions in the basis set when studying the upper valence region of the spectrum. The Rydberg states were found to be excellently represented by STO-6G functions. The overall accurate representation required both the inclusion of accurate Rydberg functions as well as augmentation of the valence basis functions. The most accurate basis set was composed of 4s, 3p and 2d functions on each center plus STO-6G functions to represent the 3s, 3p, 3d and 4s Rydberg states of Li. The largest error between the calculated and experimental atomic energies using this basis set was 0.05 eV for the neutral $^2D(3d) + ^1S$ state and 0.18 eV for the ionic $^1S + ^1P$ state.

A configuration selection scheme (CSS) comprised of a total of 7407 configurations corresponding to the configurations of the full valence CI, all Rydberg states configurations and all configurations corresponding to single excitations with respect to each Rydberg state was used to calculate the atomic states of LiBe. These were in excellent agreement with those of the full CI, indicating that the Rydberg states of the Li atom are truly SCF-like. Results obtained using this type of CSS are comparable in accuracy to those of the full CI while reducing the computational complexity. The SOCI procedure used in this study has been shown to yield highly accurate results for systems where a full CI or use of a comparable CSS is feasible.

Acknowledgments

This research was supported in part by grants from the National Science Foundation CHE-8912674 (W.C.E.) and CHE-720759 (V.E.B.) and from the Air Force Office of Scientific Research (W.C.E). The Ohio Supercomputer Center is acknowledged for a grant of Cray Y-MP time and partial support of W.C.E. Pacific Northwest Laboratory is operated for the U. S. Department of Energy Battelle Memorial Institute under Contract No. DE-AC06-76RLO 1830.

References

1. E.R. Bernstein, ed., Atomic and Molecular Clusters, (Elsevier, New York, 1990).
2. P. Jena, B.K. Rao, and S.N. Khanna, eds., Physics and Chemistry of Small Metal Clusters, (Plenum Press, New York, 1987).
3. V.E. Bondybey and J.H. English, *J. Chem. Phys.* 74, 6978 (1981).
4. M. Krauss and W.J. Stevens, *Ann. Rev. Phys. Chem.* 35, 357 (1984).
5. K. Balasubramanian, *J. Phys. Chem.* 93, 6585 (1989).
6. W.C. Ermler, R.B. Ross, and P.A. Christiansen, *Adv. Quantum Chem.* 19, 139 (1988).
7. W.C. Ermler, Y.S. Lee, P.A. Christiansen and K.S. Pitzer, *Chem. Phys. Lett.* 81, 70 (1981).
8. P.A. Christiansen, K. Balasubramanian and K.S. Pitzer, *J. Chem. Phys.* 76, 5087 (1982).
9. R.M. Pitzer and N.W. Winter, *J. Phys. Chem.* 92, 3061 (1988).
10. P.A. Christiansen, Y.S. Lee and K.S. Pitzer, *J. Chem. Phys.* 71, 4445 (1979).
11. J.P. Desclaux, *Computer Phys. Commun.* 9, 31 (1975).
12. Y.S. Lee, W.C. Ermler and K.S. Pitzer, *J. Chem. Phys.* 67, 5861 (1977).
13. L.F. Pacios and P.A. Christiansen, *J. Chem. Phys.* 82, 2664 (1985).
14. W. J. Pietro, B-A. Levi, W.J. Hehre and R.F. Stewart, *Inorg. Chem.* 19, 2225 (1980).
15. W.B. England, W.C. Ermler and A.C. Wahl, *J. Chem. Phys.* 66, 2336 (1977).

16. C.E. Moore, NBS Circ. 467, Vol 1, (1971).
17. H.M. Hulburt and J.O. Hirshfelder, J. Chem. Phys. 9, 61 (1941); J. Chem. Phys. 35, 1901 (1961).
18. See: R. Shepard, I. Shavitt, P.M. Comeau, M. Pepper, H. Lischka, P.G. Szalary, R. Ahlrichs, F.B. Brown and J.G. Zhao, Int. J. Quantum Chem., 22, 149 (1988).
19. K. Pak, W.C. Ermler, C.W. Kern and V.E. Bondybey, J. Cluster Sci., in press.
20. I. Fischer, V.E. Bondybey, P. Rosmus and H.-J. Werner, private communication.
21. C.W. Bauschlicher, S.R. Langhoff and H. Partridge, private communication.
22. G. Pichler, A.M. Lyyra, P.D. Kleiber, W.C. Stwalley, R. Hammer, K.M. Sando and H.H. Michels, Chem. Phys. Lett. 156, 467 (1989).

Table I. Basis sets of Gaussian-type functions.^a

Basis Set	Li	Be
1	(6s5p1d)/[2s2p1d] ^b	(6s5p1d)/[2s2p1d] ^b
2	(7s5p1d)/[3s2p1d] ^c	(6s5p1d)/[2s2p1d] ^b
3	(7s5p1d)/[4s2p1d] ^d	(6s5p1d)/[2s2p1d] ^b
4	(12s5p1d)/[4s2p1d] ^e	(6s5p1d)/[2s2p1d] ^b
5	(18s11p7d)/[5s3p2d] ^f	(6s5p1d)/[2s2p1d] ^b
6	(18s11p8d)/[6s4p3d] ^g	(6s5p2d)/[4s3p2d] ^h

^a Parentheses (brackets) designate primitive (contracted) basis sets.

^b Valence basis set plus one polarization function.

^c Basis set 1 plus one diffuse s-type function.

^d Basis set 2 whereby one valence s-type function has been uncontracted.

^e Basis set 3 whereby the diffuse s-type function has been replaced by one STO-6G 4s Rydberg function.

^f Basis set 4 plus three additional STO-6G Rydberg functions, one each to describe the 3s, 3p, and 3d Rydberg atomic orbitals.

^g Basis set 5 whereby one additional polarization function has been added and the valence basis functions have been uncontracted from [3s2p] to [4s3p].

^h Basis set 1 whereby one additional polarization function has been added and the valence basis functions have been uncontracted from [2s2p] to [4s3p].

Table II. Exponents and coefficients of the STO-6G Gaussian expansions of Slater-type orbitals representing the Rydberg states of LiBe.

Orbital	Exponent (ζ) ^a	Exponent (α) ^b	Coefficient ^c
3s	0.14825	0.40480	-0.00974
		0.11656	-0.07266
		0.04585	-0.17162
		0.02096	0.12898
		0.01043	0.72886
		0.00535	0.30133
3p	0.11436	0.31226	-0.00810
		0.08991	-0.01715
		0.03535	0.07370
		0.01616	0.39651
		0.00804	0.49781
		0.00413	0.11748
3d	0.11110	0.30335	0.00663
		0.08735	0.05958
		0.03435	0.24019
		0.01570	0.46481
		0.00781	0.34341
		0.00401	0.05389
4s	0.07712	0.10529	0.00378
		0.03388	-0.05586
		0.01447	-0.31930
		0.00722	-0.02765
		0.00390	0.90492
		0.00217	0.34063

^a Slater exponent,

^b Gaussian exponent,

^c Ref. 14,

Table III. Energies of LiBe and LiBe⁺ at the dissociative limit.^a

Root No.	Atomic ^b States	Full SOCI ^c	Expt. ^d	error ^e
1	2S + 1S	0.0000		
2	2P _{1/2} + 1S	1.8439	1.8478	0.0039
3-4	2P _{3/2} + 1S	1.8439	1.8478	0.0039
5	2S + 3P ₀	2.7666	2.7250	0.0416
6-8	2S + 3P ₁	2.7667	2.7251	0.0416
9-13	2S + 3P ₂	2.7669	2.7254	0.0415
14	2S (3s) + 1S	3.3325	3.3730	0.0405
15	2P _{1/2} (3p) + 1S	3.7974	3.8342	0.0368
16-17	2P _{3/2} (3p) + 1S	3.7975	3.8342	0.0367
18-19	2D _{3/2} (3d) + 1S	3.8288	3.8785	0.0497
20-22	2D _{5/2} (3d) + 1S	3.8288	3.8785	0.0497
23	2S (4s) + 1S	4.3153	4.3408	0.0454
1	1S + 1S	5.3408	5.3879	0.0471
2	1S + 3P ₀	8.1075	8.1129	0.0054
3-5	1S + 3P ₁	8.1075	8.1130	0.0055
6-10	1S + 3P ₂	8.1077	8.1133	0.0056
11	2S + 2S	9.3383	9.3224	0.0159
12-14	1S + 1P ₁	10.8476	10.6689	0.1787
15	2P _{1/2} + 2S	11.1822	11.1702	0.0120
16-17	2P _{3/2} + 2S	11.1822	11.1702	0.0120

^a Energies are in eV. The dissociative limits are 40 bohr for LiBe and 10⁶ bohr for LiBe⁺.

^b First and second entries correspond to Li and Be, respectively.

^c Basis set 6 of Table I.

^d Ref. 15.

^e Absolute values of the energy differences between entries in columns 3 and 4.

Table IV. Molecular constants of electronic states of LiBe and LiBe⁺.

State	R_e^a	D_e^b	ω_e^c	$\omega_e x_e^c$	B_e^c	α_e^c	G_0^c	T_e^c
X $2\Sigma^+$	4.95	0.25	298	9.8	0.622	0.021	146	--
A 2Π	4.27	1.50	491	3.6	0.838	0.0092	245	4768
B $2\Sigma^+$	4.91	0.89	345	2.0	0.633	0.0077	172	9745
C 2Π	5.77	0.64	191	-0.25	0.459	0.0075	96	19138
a 4Π	4.74	0.60	360	4.9	0.680	0.012	179	19525
D $2\Sigma^+$	6.73	0.30	160	7.1	0.337	-0.046	85	21884
b $4\Sigma^-$	3.99	2.03	495	3.4	0.961	0.012	247	22836
$2\Sigma^+(3s)$	5.23	0.59	383	9.2	0.558	0.011	188	24173
$2\Sigma^+(3p)$	5.10	0.68	257	2.2	0.587	0.016	129	27157
$2\Pi(3p)$	4.76	0.63	356	6.7	0.673	0.013	176	27583
$2\Delta(3d)$	4.89	0.53	300	0.35	0.638	0.0081	151	28654
$2\Pi(3d)$	5.60	0.47	211	3.1	0.487	-0.034	106	29113
$2\Sigma^+(3d)$	4.81	0.38	357	5.0	0.660	0.013	177	29805
$2\Sigma^+(4s)$	5.03	0.52	302	6.0	0.603	0.011	149	32426
X $1\Sigma^+$	4.98	0.56	311	4.8	0.616	0.013	154	--
a $3\Sigma^+$	5.58	0.91	274	2.2	0.490	0.006	137	19476
b 3Π	5.09	0.19	235	7.0	0.590	0.021	116	25332

a bohr.

b eV.

c cm⁻¹.

Table V. Excitation energies (eV) showing effects of basis set on the Rydberg states of LiBe at the dissociative limit (40 bohr) using full SOCI.

Root ^a	Basis Set 1	Basis Set 2	Basis Set 3	Basis Set 4	Basis Set 5
1	0.0000	0.0000	0.0000	0.0000	0.0000
2	1.8389	1.8389	1.8417	1.8417	1.8419
3	1.8389	1.8389	1.8417	1.8417	1.8419
4	1.8389	1.8389	1.8417	1.8417	1.8419
5	2.7761	2.7762	2.7761	2.7764	2.7764
6	2.7765	2.7765	2.7765	2.7765	2.7765
7	2.7765	2.7765	2.7765	2.7765	2.7765
8	2.7765	2.7765	2.7765	2.7765	2.7765
9	2.7767	2.7767	2.7767	2.7767	2.7767
10	2.7767	2.7767	2.7767	2.7767	2.7767
11	2.7767	2.7767	2.7767	2.7767	2.7767
12	2.7767	2.7767	2.7767	2.7767	2.7767
13	2.7767	2.7767	2.7767	2.7767	2.7767
14	4.3889	3.8779	3.4179	3.3682	3.3354
15	4.3889	4.3889	4.3169	4.3508	3.7987
16	4.3889	4.3889	4.3916	4.3916	3.7987
17	--	4.3899	4.3916	4.3917	3.7987
18	--	--	4.3917	4.3917	3.8268
19	--	--	--	--	3.8268
20	--	--	--	--	3.8268
21	--	--	--	--	3.8268
22	--	--	--	--	3.8268
23	--	--	--	--	4.3153

^a Refer to Table III for state designations.

Table VI. LiBe excitation energies (eV) corresponding to SOCI wavefunctions defined using two configuration selection schemes (CSS).^a

Root ^b	Atomic State	SOCI/CSS1 ^c	SOCI/CSS2 ^d	Full SOCI ^e
1	2S + 1S	0.0000	0.0000	0.0000
2	2P _{1/2} + 1S	1.8419	1.8419	1.8419
3-4	2P _{3/2} + 1S	2.0595	1.8419	1.8419
5	2S + 3P ₀	2.7765	2.7764	2.7765
6-8	2S + 3P ₁	2.7765	2.7765	2.7765
9-13	2S + 3P ₂	2.7767	2.7767	2.7767
14	2S (3s) + 1S	4.5655	3.3354	3.3354
15	2P _{1/2} (3p) + 1S	---	3.7987	3.7987
16-17	2P _{3/2} (3p) + 1S	---	3.7987	3.7987
18-19	2D _{3/2} (3d) + 1S	---	3.8269	3.8268
20-22	2D _{5/2} (3d) + 1S	---	3.8269	3.8268
23	2S (4s) + 1S	---	4.3154	4.3153
24	2P _{1/2} + 3P ₀	4.6183	4.6183	4.6183
25-27	2P _{1/2} + 3P ₁	4.6183	4.6183	4.6183
.
50	2P _{3/2} + 3P ₂	4.6523	4.6187	4.6187

^a Roots 24 through 50 are double excitation states of LiBe. Only the first four and the last of these states are shown.

^b All calculations were accomplished at 40 bohr using a triple zeta (double zeta) s, double zeta (double zeta) p and single zeta (single zeta) d valence basis set on Li (Be) plus 3s, 3p, 3d and 4s STO-6G functions to represent Rydberg states of Li (Basis set 5 in Table I).

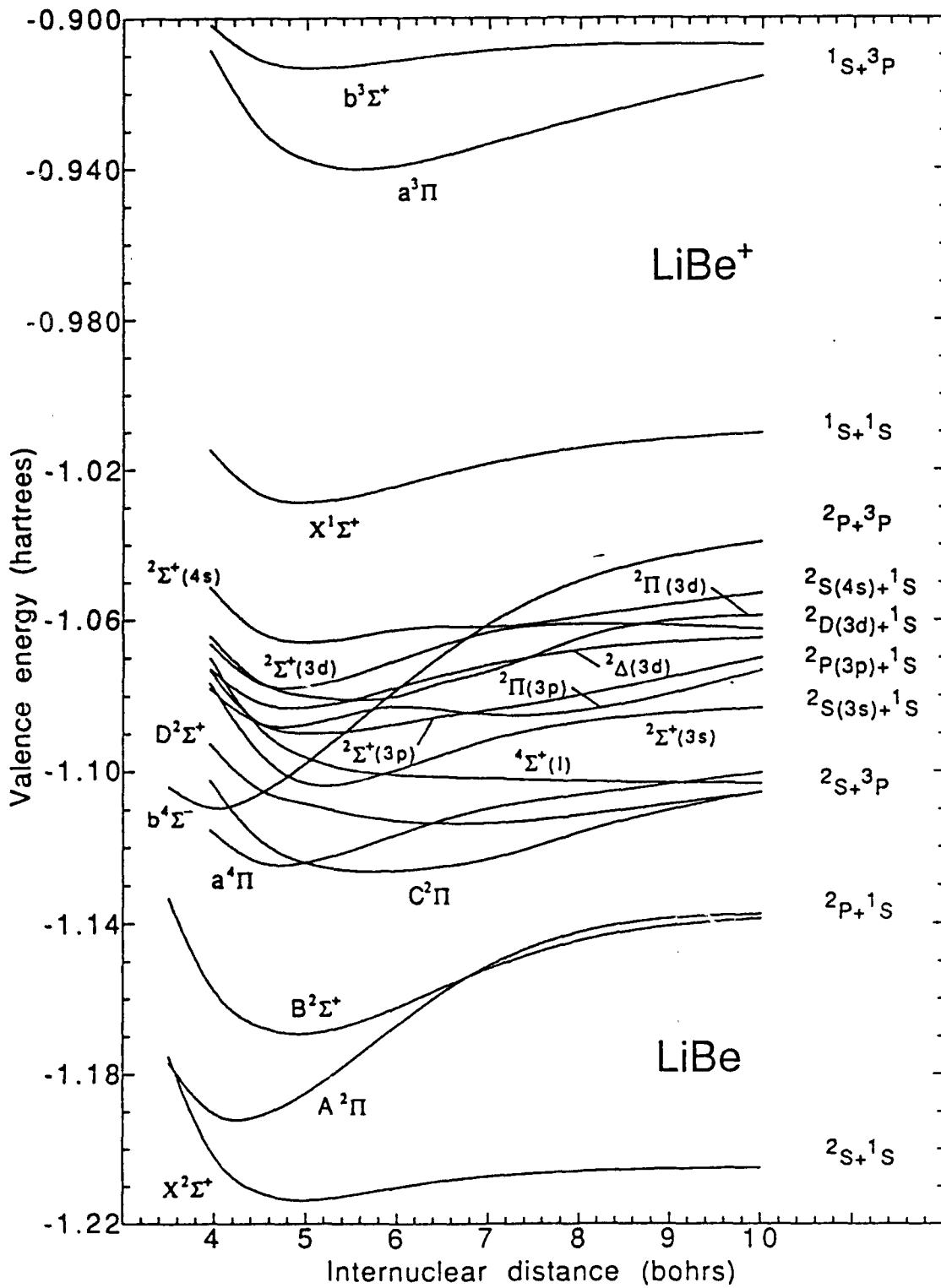
^c 4072 configurations. Includes full valence SOCI plus Rydberg state configurations.

^d 7407 configurations. Includes full valence SOCI, Rydberg state configurations and all single excitations relative to Rydberg states where no more than one electron occupies a particular Rydberg orbital for any given configuration.

^e 9102 configurations.

Figure captions

- Figure 1. Potential energy curves of valence and Rydberg states of LiBe and of three states of LiBe^+ . Asymptotic atomic states are Li and Be, respectively.
- Figure 2. Selected potential energy curves of LiBe plotted on an expanded energy scale relative to that of Fig. 1.



AB INITIO REP-BASED RELATIVISTIC CORE/VALENCE POLARIZATION OPERATOR

M. M. Marino and W. C. Ermler

Molecular Science Research Center
Pacific Northwest Laboratory
Richland, Washington 99352

and

Department of Chemistry and Chemical Engineering
Stevens Institute of Technology
Hoboken, New Jersey 07030

INTRODUCTION

Core polarization is an effect due to the correlation between electrons in the valence space and those in the core region. As a result of this correlation, valence electrons are affected by the instantaneous positions of the core electrons, and the simple concept of core-valence separability breaks down as the magnitude of this correlation phenomenon increases. Core polarization is greatest for systems containing a small number of valence electrons and having cores that are polarized easily.

Born and Heisenberg presented a treatment of the core polarization effect for atoms containing a single valence electron.¹ Mayer and Mayer² and van Vleck and Whitelaw³ later presented improved core/valence polarization potentials. However, the potentials were not properly behaved at short electron-nucleus distances, leading Bierman⁴, Bierman and Lubeck⁵ and Bates⁶ to introduce empirical cut-off functions to address the problem. Since these developments a large number of researchers have further contributed by discussing - among many related topics - two-electron interactions, non-adiabatic corrections, and theoretical potentials using non-empirical functions, as well as presenting a host of applications.⁷ Muller et al.⁷ have presented a procedure whereby the core polarization is described by a semi-empirical potential used in all-electron SCF and valence CI calculations.

Stoll et al. have used their method in pseudopotential calculations.⁸ Christiansen⁹ later paralleled the procedure of Muller et al. to develop an ab initio core/valence polarization potential (CVPP) in the context of the adiabatic field approximation^{10,11} and relativistic effective potential (REP) theory.¹²

The latter CVPP has several advantages. First, the procedure is non-empirical. Second, relativistic effects are incorporated. Third, the valence space is reduced to include the smallest possible number of electrons. The last two points, which are extremely important, result from derivation of the CVPP within the REP approximation.

REP-based methods rely on the principle of core/valence separability. Consequently, a choice must be made regarding the number of electrons to be treated explicitly. In the procedure developed by Lee et al.¹², this choice is arbitrary. For example, the most practical REP for cesium would correspond to a one-electron valence space. The same atom may also be described by 9-electron and 19-electron valence spaces, where the former REP contains the 5s and 5p Cs electrons in the valence space and the latter contains a valence space comprised of the 5s, 5p and 4d electrons. A one-electron-valence-space REP would allow the minimum number of electrons to be treated explicitly and, therefore, would render calculations at, say, the full configuration interaction (CI) level possible for clusters of two or more Cs atoms. However, such an REP yields inaccurate excitation and ionization energies for Cs because of the large effects of core/valence polarization in this atom.¹³ To improve accuracy, a 9-electron-valence-space REP may be used, although this would obviously render full CI calculations, or even procedures that incorporate modest levels of electron correlation, intractable. There is a second disadvantage to using a larger valence space REP. Because the REPs are generated using Dirac-Fock theory, relativistic effects are incorporated into REP-based calculations via the core electrons. Relativistic effects in the valence region, which is treated non-relativistically, result from the propagation of these effects from the core to the valence electrons.¹⁴ Thus, a reduction in the number of core electrons results in a loss of relativistic effects, leading to decreased accuracy for calculations on heavy-element systems where such effects are increasingly important. Christiansen showed that a high level of accuracy may be achieved with the minimum-valence-electron REP if a CVPP is included in the calculations.⁹

This paper extends the method presented by Christiansen to an REP-based CVPP derived in *j-j* coupling. Here, the relativistic CVPP (RCVPP) is calculated using individual orbital contributions rather than total energies, making it possible to see the effect of each orbital on the total potential.

METHOD

Since the formal derivation of the REPs is given in Refs. 12 and 14, only those relationships relevant to the RCVPP development are given here. The REPs, which are based on numerical Dirac-Fock (DF) wavefunctions¹⁵, are expressed as follows:

$$U_{\text{REP}} = U_{\text{L}}^{\text{REP}}(r) + \sum_{l=0}^{L-1} \sum_{j=|l-1/2|}^{l+1/2} \sum_{m=-j}^j [U_{lj}^{\text{REP}}(r) - U_{\text{L}}^{\text{REP}}(r)] |ljm\rangle\langle ljml| \quad (1)$$

where the projection operators $|ljm\rangle\langle ljml|$ dictate that U^{REP} must be used in the context of a basis set of two-component Dirac spinors.¹⁶ The REPs can be recast into the form of an angular momentum averaged potential that may be used in the context of standard nonrelativistic electronic structure procedures based on atomic L-S coupling and a spin-orbit operator.¹⁴ This AREP is defined by

$$U_{\text{AREP}} = U_{\text{L}}^{\text{AREP}}(r) + \sum_{l=0}^{L-1} \sum_{m=-l}^l [U_{lj}^{\text{AREP}}(r) - U_{\text{L}}^{\text{AREP}}(r)] |lm\rangle\langle lml| \quad (2)$$

where

$$U_{\text{L}}^{\text{AREP}} = (2l+1)^{-1} [l U_{l,l-1/2}^{\text{REP}} + (l+1) U_{l,l+1/2}^{\text{REP}}] \quad (3)$$

In Eqs. (1) and (2) $U_{\text{L}}^{\text{REP}}$ and $U_{\text{L}}^{\text{AREP}}$ refer to the so called "residual" EPs where L, J and L are normally taken as one larger than the largest angular momentum quantum numbers among the core electrons.

The resulting spin-orbit operator is

$$H^{\text{SO}} = S \cdot \sum_{l=1}^L [2/(2l+1)] \Delta U_{lj}^{\text{REP}}(r) \sum_{m=-l}^l |lm\rangle\langle lml| |lm\rangle\langle lml| \quad (4)$$

where

$$H_{lj}^{\text{SO}} = [2/(2l+1)] \Delta U_{lj}^{\text{REP}}(r) \quad (5)$$

and

$$\Delta U_{\text{L}}^{\text{AREP}}(r) = U_{l,l-1/2}^{\text{AREP}} - U_{l,l+1/2}^{\text{AREP}} \quad (6)$$

Although U_{lj}^{REP} , U_{lj}^{AREP} , and H_{lj}^{SO} are derived as numerical operators, consistent with their origin from numerical DF wavefunctions, they are re-expressed as expansions in terms of Gaussian functions in the following form:

$$O_k(r) = r^{-2} \sum_{i=1}^M C_{ki} \cdot (r_{ki}) e^{-\alpha_{ki} r^2}, \quad O_k(r) = U_{lj}^{\text{REP}}, U_{lj}^{\text{AREP}}, \text{ or } H_{lj}^{\text{SO}} \quad (7)$$

The RCVPP is defined in the context of the adiabatic field approximation and the REP of Eq. (1). The total core polarization potential operator is,⁸

$$V_{\text{RCVPP}} = -1/2 \sum_c \alpha_c f_c f_c \quad (8)$$

where α_c is the polarizability of the outer core of atom c and f_c is the electric field at the nucleus due to the valence electrons and the other atomic cores. If an adiabatic potential is defined as

$$V_{RCVPP}^{nd}(r) = E_{pol}(r) - E_{ion}(r) \quad (9)$$

Where E_{ion} and E_{pol} are the energy of the atom in the field of a point charge placed at r before and after, respectively, orbital (self-consistent) relaxation calculated using a relativistic procedure. The RCVPP can then be defined as

$$V_{RCVPP}(r) = C(r_{ci}) V_{RCVPP}^{nd}(r) \quad (10)$$

In Eq. (10) the fraction of core electron density within the valence radius is

$$C(r_{ci}) = 1/N_c \sum_{k=1}^{N_c} \int_0^{r_{ci}} |\phi_k(r)|^2 dr \quad (11)$$

where ϕ_k are the N_c normalized radial numerical DF core orbitals.⁹

The effective field at the core of atom c is then

$$f_c(r_{ci}) = (r_{ci}/r_{ci}) [2C(r_{ci}) V_{RCVPP}^{nd}(r) / \alpha_c]^{1/2} \quad (12)$$

which leads to the following form:

$$\begin{aligned} V_{RCVPP} = & 1/2 \sum_i \alpha_c [\sum_i f_c(r_{ci})^2 + \sum_j f_c(r_{ci}) \cdot f_c(r_{ij}) \\ & - 2 \sum_j \sum_{c'} f_c(r_{ci}) \cdot (R_{cc'}/R_{cc'^3}) Z_{c'} \\ & + \sum_{c',c''} (R_{cc'} \cdot R_{cc''}) / (R_{cc'^3} R_{cc''^3}) Z_{c'} Z_{c''}] \end{aligned} \quad (13)$$

where

$$\alpha_c = -2r^4 \Delta E_{pol}/q^2 \quad (14)$$

and α_c is the polarizability (see Eq. 8), q the point charge at a distance r from the nucleus and ΔE_{pol} the change in energy (V_{RCVPP}^{nd}) due to polarization of the outer core orbitals by the point charge. In Eq. (13) the terms one through four are the one-center one-electron contributions, one-center two-electron contributions, electron-other-core interactions, and core-core interactions, respectively. Z_c is the charge on core c . It is noted that substituting Eq. 12 into Eq. 13 results in the cancellation of α_c from the first term - the one-center one-electron contribution.

Up to this point the development of the core/valence polarization potential V_{RCVPP} is the same as that in Ref. 10 for the nonrelativistic treatment. We will now show how the

V_{RCVPP} can be derived from individual orbital contributions. The total energies $E_{pol}(R)$ and $E_{ion}(R)$ given in Eq. 9 can be expressed¹⁷ as

$$E_{pol}(r) = \sum_i (\epsilon_i + H_{ii}) + Z_c Z' / r \quad (15)$$

and

$$E_{ion}(r) = \sum_i (\epsilon_i^0 + H_{ii}^0) + Z_c Z' / r \quad (16)$$

where ϵ_i and H_{ii} are the orbital energy and one-electron energy, respectively, corresponding to a system comprised of an atom in the field of an electron or point charge with $Z' = -1$. ϵ_i^0 and H_{ii}^0 are the orbital energy and one-electron energy, respectively, corresponding to this same system but before self-consistent orbital relaxation occurs; the orbitals in this case correspond to field-free atomic orbitals, i.e. without the presence of the point charge. $Z_c Z' / r$ is the interaction potential the atomic nucleus and the point charge. Since Z' corresponds to a point charge (electron), $Z_c Z' / r$ becomes $-Z_c / r$. Substituting Eqs. 15 and 16 into Eq. 9 yields

$$V_{RCVPP}^{nd}(r_{ci}) = (\epsilon_i + H_{ii}) - (\epsilon_i^0 + H_{ii}^0) \quad (17)$$

and

$$V_{RCVPP}^{nd}(r_{ci}) = \sum_i V_{RCVPP}^{nd}(r_{ci}) \quad (18)$$

It is noted that two-electron interactions are present via ϵ_i and ϵ_i^0 since

$$\epsilon_i = H_{ii} + \sum_j (2J_{ij} - K_{ij}) \quad \text{and} \quad \epsilon_i^0 = H_{ii}^0 + \sum_j (2J_{ij}^0 - K_{ij}^0) \quad (19)$$

where J_{ij} and K_{ij} are the coulomb and exchange integrals, respectively.¹⁷ Further,

$$H_{ii}^0 = H_{ii}^{atom} + V_{ip}^0 \quad (20)$$

and

$$\epsilon_i^0 = \epsilon_i^{atom} + V_{ip}^0 \quad (21)$$

where

$$V_{ip}^0 = \langle \phi_i^0 | -Z_c / r_{ci} | \phi_i^0 \rangle \quad (22)$$

ϕ_i^0 are atomic orbitals and ϵ_i^{atom} are the orbital energies corresponding to the unperturbed

atom. i.e., the only difference between the unrelaxed orbital energies in the presence of the point charge and the atomic orbital energies is the attractive potential between the negative point charge and the positive nucleus.

Substituting Eqs. 20 and 21 into Eq. 17 yields

$$V_{\text{RCVPP}}^{\text{ad}}(r) = \sum_i (\epsilon_i - \epsilon_i^{\text{atom}} + H_i - H_{ii}^{\text{atom}} - 2V_{\text{ip}}^0) \quad (23)$$

Eq. 23, which defines $V_{\text{RCVPP}}^{\text{ad}}(r)$ appearing in Eq. 10, shows that V_{RCVPP} can be calculated from the orbital energies and one-electron energies corresponding to relaxed relativistic atomic orbitals in the field of a negative point charge (ϵ_i and H_{ii} , respectively), and the orbital energies and one-electron energies of the unperturbed atom (ϵ_i^{atom} and H_{ii}^{atom} , respectively) plus the attractive potential energy between the nucleus and the point charge (V_{ip}^0).

CALCULATIONS

The $V_{\text{RCVPP}}^{\text{ad}}(\text{total})$ shown in Figs. 1 and 2 and the $V_{\text{RCVPP}}(\text{total})$ in Fig. 3 were calculated from the total energies E_{pol} and E_{ion} (see Eq. 9) using the method of Christiansen.⁹ The same values were also calculated from the individual $V_{\text{RCVPP}}^{\text{ad}}(r)_i$ and Eqs. 18 and 23. As expected, the two methods yield identical results. The $V_{\text{RCVPP}}^{\text{ad}}(r)_i$ appearing in Figs. 1 and 2 and the $V_{\text{RCVPP}}(r)_i$ appearing in Fig. 3 were calculated from respective cesium ion energies defined by Eqs. 17-22.

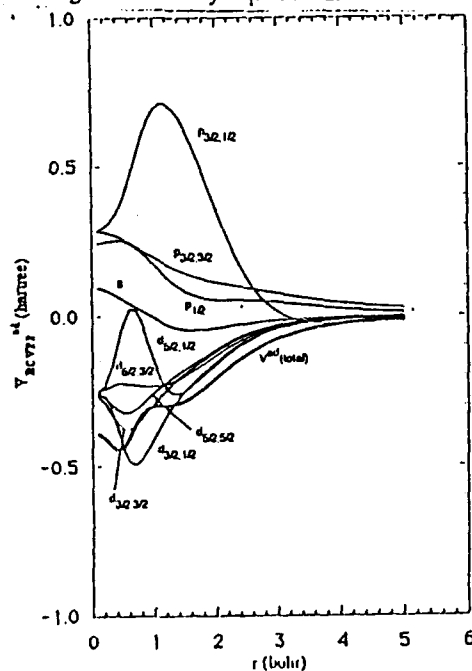


Figure 1. Total adiabatic potential and its individual lj, m_j contributions for Cs.

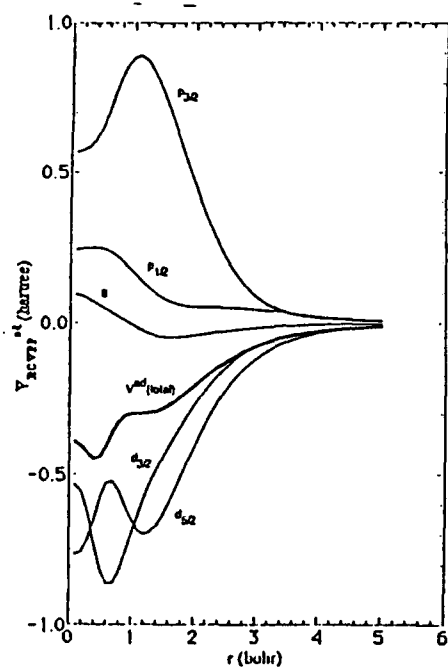


Figure 2. Total adiabatic potential and its individual $l j$ contributions for Cs.

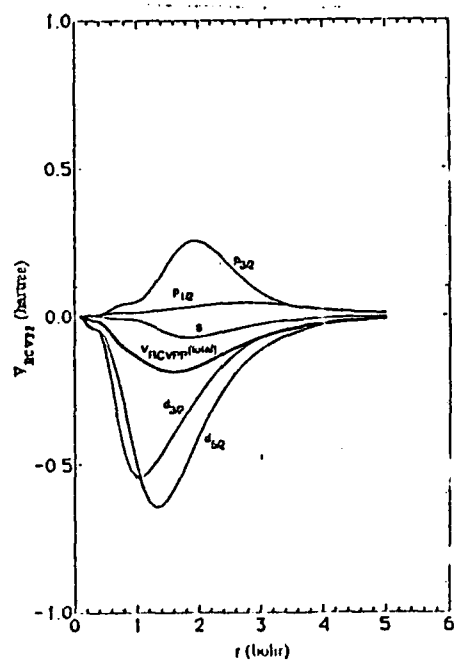


Figure 3. Total relativistic core/valence polarization potential and its individual $l j$ contributions for Cs.

The Cs⁺ orbital space was partitioned as follows. The 1s-4s; the m=1/2 and 3/2 components of the 2p-4p; and the m=1/2, 3/2 and 5/2 components of the 3d orbitals defined the core space and were described by an REP derived¹¹ from the orbitals of a singly-charged Cs positive ion defined as having 18 valence electrons. The 4d_{3/2}, 4d_{5/2}, 5s, 5p_{1/2} and 5p_{3/2} orbitals were treated as outer core (or inner valence) and the 6s electron, comprised the valence space. A basis set of three 5s, two 6s, three 5p_{1/2} and 5p_{3/2}, two 6p_{1/2} and two 6p_{3/2}, two 4d_{5/2} and two 4d_{3/2}, two 5d_{5/2} and two 5d_{3/2}, and two 4f_{7/2} and two 4f_{5/2} Slater-type functions was used to describe these orbitals. The 6s electron was ionized and the effects of polarization by a negative point charge on the 4d_{3/2}, 4d_{5/2}, 5s and 5p_{1/2} outer core orbitals of Cs⁺ were determined by calculation of E_{pol} and E_{ion} of Eq. 9 from the individual orbital energies (refer to Eqs. 17-22), resulting in the generation of a RCVPP through which these effects are described. Once the RCVPP is determined, it can be used in calculations where the 4d_{3/2}, 4d_{5/2}, 5s, 5p_{1/2} and 5p_{3/2} electrons of Cs are considered part of the core and described by a one-valence-electron (6s) REP to which the RCVPP is added, thereby reducing to one the number of valence electrons treated explicitly. This procedure considers core/valence polarization to be an atomic property. Hence, once the RCVPP is generated, it can be used to describe the structure of Cs in any bonding situation and any electronic states involving excitation of the Cs 6s valence electron.

A relativistic diatomic molecule program system was used to obtain the energy corresponding to each valence orbital.¹⁶ It is based in ω - ω coupling¹⁸ and yields wavefunctions that are eigenfunctions of the total angular momentum squared operator, making it possible to calculate a V_{RCVPP} for each j and m_j component. The one-electron and attractive potential energies were calculated using codes developed specifically for this purpose. Eq. 17 was then used to obtain each V_{RCVPP^{ad}}(r)_i. The set of C(r_a)_i given by Eq. 11 were calculated using the normalized radial numerical Dirac-Fock core orbitals ϕ_k .¹⁵ These same orbitals were used to derive the 18-valence electron REP employed here. The polarizability, α_c of Eq. 14, which is a constant for sufficiently large r, was calculated by taking r as 20 bohrs. The final V_{RCVPP} was calculated using Eqs. 23 and 10-14.

DISCUSSION

There are advantages to deriving V_{RCVPP} from the relativistic atomic orbitals rather than from the total energy. First, the former method allows the contributions of the V_{RCVPP}(r)_i's to the total V_{RCVPP} to be studied individually, while the latter one does not. Second, the calculations are carried out in the j-j coupling scheme, thereby making it possible to determine contributions of V_{RCVPP} to the spin-orbit splitting energies. Figure 1 shows the behavior of each ljm component of V_{RCVPP^{ad}}(r). The five V_{RCVPP^{ad}}(r)_{ljm} shown in Fig. 2 were obtained by summing over the m components of each V_{RCVPP^{ad}}(r)_{ij} (see Fig. 1). The total sum of the five potentials in Fig. 2 and the potential generated from the total energy of the system [V_{RCVPP^{ad}}(total)], which are identical, are also shown in the figure. Figure 3 shows the

individual $V_{RCVPP}(r)_{ij}$ calculated from Eq (10) and the $V_{RCVPP}^{nd}(r)_{ijm}$ of Fig. 2. The $V_{RCVPP}(total)$, which was generated from the individual orbital energies, is also included.

Since the complete V_{RCVPP}^{nd} is essentially the energy difference between the relaxed and unrelaxed orbitals in the presence of the point charge [multiplied by the cut-off function, of course, in the case of $V_{RCVPP}(r)_i$], a positive $V_{RCVPP}^{nd}(r)_i$ for a given orbital indicates that the orbital is destabilized by the charge, while a negative $V_{RCVPP}^{nd}(r)_i$ indicates a stabilization of the orbital due to the presence of the point charge. Comparing the $V_{RCVPP}(r)_{ijm}$ and $V_{RCVPP}^{nd}(total)$ in Fig. 1, it is clear that many of the details relating to orbital behavior in the presence of the point charge are lost if V_{RCVPP} is calculated from the total energies rather than from the individual orbital energies. This figure shows that the $p_{3/2,3/2}$ and $p_{3/2,1/2}$ orbitals, which are degenerate at $r=\infty$ (no perturbation due to the point charge), polarize differently. The $p_{3/2,1/2}$ orbital is more sensitive to the point charge than the $p_{3/2,3/2}$. The positive values of $V_{RCVPP}^{nd}(r)_{p_{3/2,3/2}}$ and $V_{RCVPP}^{nd}(r)_{p_{3/2,1/2}}$ indicate that the corresponding orbitals are destabilized by the point charge. On the other hand, the orbitals corresponding to $V_{RCVPP}^{nd}(r)_{d_{5/2,5/2}}$, $V_{RCVPP}^{nd}(r)_{d_{5/2,3/2}}$ and $V_{RCVPP}^{nd}(r)_{d_{5/2,1/2}}$ are all stabilized strongly by the field due to the point charge (relative to the other $V_{RCVPP}^{nd}(r)_{ijm}$ of Fig. 1) since these all have negative values. However, the differences among these orbitals are not large for $r > 1.6$ bohr. At smaller r , the behavior of $V_{RCVPP}^{nd}(r)_{ijm}$ for the d orbitals is mostly dictated by the $d_{5/2,1/2}$ component, which is not affected by the point charge at $r = 0.8$ bohr. It is noted that multiplication of each $V_{RCVPP}^{nd}(r)_i$ by the cut-off function will alter the behavior of these potentials at small r ; this is discussed further on. The $d_{3/2,1/2}$ orbital is also stabilized by polarization and reacts similarly to the $d_{3/2,3/2}$ orbital, causing the two corresponding $V_{RCVPP}^{nd}(r)_i$ to be similar in shape, although the $d_{3/2,3/2}$ component is slightly more stabilized. The nondegenerate s and $p_{1/2}$ orbitals also react similarly to the point charge, but whereas the effect on the former is almost negligible, the latter is somewhat destabilized.

The sum of the m components of each $V_{RCVPP}^{nd}(r)_{ijm}$ appear in Fig 2. Since the s and $p_{1/2}$ orbitals are degenerate, there is no difference between their corresponding $V_{RCVPP}^{nd}(r)_{ij}$ and $V_{RCVPP}^{nd}(r)_{ijm}$. The $d_{5/2}$ and $p_{3/2}$ orbitals, on the other hand, react strongly to the presence of the point charge, with the $d_{5/2}$ orbital being more affected by the polarization process. A comparison of Figs. 1 and 2 indicates that the value of V_{RCVPP}^{nd} for $p_{3/2}$ largely arises from the behavior of the $p_{3/2,1/2}$ component. The maximum at small r in the curve corresponding to the $d_{5/2}$ orbital is due to $V_{RCVPP}^{nd}(r)_{d_{5/2,3/2}}$. From Fig. 2 it is apparent that $V^{nd}(total)$, which is the sum of each $V_{RCVPP}^{nd}(r)_{ij}$, is closer in shape to the $V_{RCVPP}^{nd}(r)_{d_{3/2}}$ and $V_{RCVPP}^{nd}(r)_{d_{5/2}}$ potentials. The total potential indicates that the overall effect of polarization by the point charge is to stabilize the Cs inner valence (outer core) orbitals, while the breakdown of $V^{nd}(total)$ clearly shows that only the d components become more stable. Both the p orbitals, on the other hand, are destabilized, with the bulk of the destabilization arising from the polarization of the $p_{3/2}$ orbital.

The individual $V_{RCVPP}^{nd}(r)_{ij}$ of Fig. 2 were multiplied by the cut-off functions, Eqs. 10-11, to ensure proper behavior as r approaches zero and the results were then plotted in Fig. 3, along with the total V_{RCVPP} obtained according to Eqs. 18, 10 and 23. The resulting

$V_{RCVPP}(total)$ differs considerably from $V^{ad}(total)$ of Fig. 2. The shape of $V_{RCVPP}(total)$ is now closer to that of the s potential than to $V_{RCVPP}(r)_{d3/2}$ and $V_{RCVPP}(r)_{d5/2}$, as was the case in Fig. 2. Multiplication by the cut-off function also results in a smoother $d_{5/2}$ potential, relative to that appearing in Fig. 2, such that the $d_{5/2}$ and $d_{3/2}$ components behave similarly. Again, the $V_{RCVPP}(r)_{p3/2}$ indicates a destabilization of its corresponding orbital with respect to polarization, although the instability is greatly reduced for $V_{RCVPP}(r)_{p3/2}$ vs. $V_{RCVPP}^{ad}(r)_{p3/2}$. The $p_{1/2}$ orbital is now only negligibly affected by the point charge, whereas the s orbital is slightly more stable relative to the unperturbed atom. Again, it is clear that the behavior of $V_{RCVPP}(total)$ mirrors the behavior of the $V_{RCVPP}(r)_s$ and, to a lesser degree, that of the $V_{RCVPP}(r)_{p1/2}$. However, it neither indicates the degree to which the $p_{3/2}$ orbital destabilizes nor the $d_{3/2}$ and $d_{5/2}$ orbitals stabilize as a result of polarization. Only the $V_{RCVPP}(r)_{lj}$ were plotted (as opposed to $V_{RCVPP}(r)_{ljm}$) because there is a one-to-one analogy between these values and the corresponding lj terms in the REP expansion. A method for incorporating $V_{RCVPP}(r)_{ljm}$ into REP-based molecular calculations is currently under investigation, although this is a more complex problem.

Having developed the procedure whereby a relativistic V_{RCVPP} is calculated for each ljm component, the potentials will be used in calculations such that each angular momentum component of the total REP has associated with it a $V_{RCVPP}(r)_{lj}$ or $V_{RCVPP}(r)_{ljm}$. The current procedure involves incorporation of the total V_{RCVPP}^{13} and not its individual components (Eq. 17). Because the individual $V_{RCVPP}(r)_i$ vary widely from the total potential, it is anticipated that incorporation of the lj or ljm components of V_{RCVPP} will improve calculational results on systems where core/valence polarization effects are important.

ACKNOWLEDGMENTS

This research was supported in part by the National Science Foundation (CHE-8912674), the Air Force Office of Scientific Research and by the Division of Chemical Sciences Office of Basic Energy Sciences, U.S. Department of Energy under contract No. DE-AC06-76RLO 1830 with Battelle Memorial Institute which operates the Pacific Northwest Laboratory.

REFERENCES

1. M. Born and W. Heisenberg, Z. Phys. 23, 388 (1924).
2. J.E. Mayer and M.G. Mayer, Phys. Rev. 43, 650 (1933).
3. J.H. van Vleck and H.G. Whitelaw, Phys. Rev. 44, 551 (1933).
4. L. Biermann, Z. Astrophys. 22, 1957 (1943).
5. L. Biermann and K. Lubeck, Z. Astrophys. 25, 325 (1948).
6. D.R. Bates, Proc. R. Soc. London Ser. A188, 350 (1947).
7. See W. Muller, J. Flesch and W. Meyer, J. Chem. Phys. 80, 3297 (1984) and references therein.
8. H. Stoll, P. Feuntealpa, P. Schwertdfeger, J. Flad, L. V. Szentpaly and H. Preuss, J. Chem. Phys. 81, 2732 (1984).
9. P.A. Christiansen, Chem. Phys. Lett. 127, 50 (1986).
10. A. Temkin and J.C. Lamkin, Phys. Rev. 121, 788 (1961).
11. A.K. Bhatia, A. Temkin, A. Silver and E.C. Sullivan, Phys. Rev. A18, 1935 (1978).
12. Y.S. Lee, W.C. Ermler and K.S. Pitzer, J. Chem. Phys. 67, 5861 (1977); P. A. Christiansen, Y.S. Lee, and K.S. Pitzer, J. Chem. Phys. 71, 4445 (1979).
13. L. LaJohn, Ph.D. dissertation, Clarkson University (1989).
14. W.C. Ermler, R.B. Ross and P.A. Christiansen, Adv. Quantum Chem. 19, 139 (1988).
15. J.P. Declaux, Compt. Phys. Commun. 9, 31 (1975).
16. Y.S. Lee, W.C. Ermler and K.S. Pitzer, J. Chem. Phys. 73, 360 (1980).
17. R.S. Mulliken and W.C. Ermler, Diatomic Molecules: Results of *ab Initio* Calculations, Academic Press, New York, 1977.
18. G. Malli and J. Oreg, J. Chem. Phys. 63, 830 (1975).

4. Publications

"On the interpretation of scanning tunneling microscope images showing anomalous periodic structures", M. Sawamura, J. F. Womelsdorf and W. C. Ermler, *The Journal of Physical Chemistry* **95**, 8823-6 (1991).

"Ab initio studies of the electronic structure and density of states of metallic beryllium", R. B. Ross, W. C. Ermler, C. W. Kern and R. M. Pitzer, *International Journal of Quantum Chemistry* **41**, 733-48 (1992).

"Spin-orbit configuration-interaction study of valence and Rydberg states of LiBe", M. M. Marino and W. C. Ermler, *The Journal of Chemical Physics* **96**, 3756-66 (1992).

"Ab initio REP-based relativistic core/valence polarization operator", M. M. Marino and W. C. Ermler, in *Proc. NATO/ASI Advanced Study Institute on Relativistic and Correlation Effects in Molecules and Solids*, Plenum, New York, in press.

"Characterization of gold sols by scanning tunneling microscopy", J. F. Womelsdorf, Ph. D. dissertation, Stevens Institute of Technology, 1993, expected.

5. Professional Personnel

Dr. Walter C. Ermler (Principal Investigator) Professor of Chemistry and Physics

Dr. Maria M. Marino, Postdoctoral Associate

Mr. John F. Womelsdorf, Graduate Research Assistant

6. Interactions

(1) Spoken Papers

Invited seminar - "Ab Initio Studies of Heavy Metal Clusters Using a Spin-Orbit Configuration Interaction Method", Department of Chemistry, Washington State University, Pullman, WA, March 30, 1992.

Invited poster - "Ab Initio Configuration Interaction Studies of Cs_2 , Cs_2^+ and $\text{Cs}(\text{H}_2\text{O})^+$ ", West Coast Theoretical Chemistry Conference, Molecular Science Research Center, Richland, WA, May, 21-23, 1992.

Invited seminar - "Program Systems for Use in Studies of Polyatomic Systems Containing Heavy Elements Using Ab Initio Methods", Molecular Science Research Center, Richland, WA, May, 1992.

Invited seminar - "Ab Initio Studies of Molecules and Clusters Using REPs", Molecular Science Research Center, Richland, WA, May, 1992.

Invited lecturer at the NATO/ASI Advanced Study Institute on "Relativistic and Electron Correlation Effects in Molecules and Solids", August 10-22, 1992, Vancouver, B. C., Canada (Two lectures and member of panel on relativistic effects.)

(2) Consultative and Advisory Functions

None

7. New Discoveries, Inventions or Patent Disclosures

None

8. Additional Statement

None